ABSTRACT

BHARAMBE, VIVEK TULSHIRAM. Analysis of Liquid Metal Vacuum Filling Approach to Develop 3D Printed Antennas. (Under the direction of Dr. Jacob J. Adams.)

This work proposes a novel method of fabrication of antennas using vacuum filling of liquid metals into three-dimensional additively manufactured hollow structures built using PolyJet printing. These hollow structures created by melting and dissolving off a sacrificial support material and ultimately filled with EGaIn can enable cost-effective fabrication of highly accurate complex 3D electromagnetic geometries and exploration of new design parameters.

It also summarizes the resonant cavity measurements for characterization of complex electrical permittivity of the printing material VisiJet M3 Crystal used to fabricate a microstrip patch antenna designed for 6 GHz. The fabricated antenna was then characterized for its gain and reflection co-efficient in an anechoic chamber for comparison to simulation results. These results demonstrate a good alignment with simulation data with around 1% deviation in the operating frequency of the antenna. In addition, more complex geometries such as helical antenna and four-element array with an integrated co-axial feed structure were designed, fabricated and characterized at 6 GHz to further prove the versatility of the process. Although the acrylic printing material, VisiJet M3 Crystal has high dielectric losses at microwave frequencies, the technique can be used with other 3D printable low-loss materials to construct highly efficient embedded antennas.

Certain issues faced during the fabrication of these antennas and the limitations of the process are also discussed.

Keywords: 3D printing, liquid metal antennas, dielectric characterization, microstrip patch array, helical antenna.

Analysis of Liquid Metal Vacuum Filling Approach to Develop 3D Printed Antennas

by
Vivek Tulshiram Bharambe

A thesis submitted to the Graduate Faculty of
North Carolina State University
in partial fulfillment of the
requirements for the degree of
Master of Science

Electrical Engineering

Raleigh, North Carolina

2017

APPROVED BY:

_____	_____
Dr. Michael Dickey	Dr. Brian Floyd

_____
Dr. Jacob J. Adams
Chair of Advisory Committee

DEDICATION

Dedicated to my family

BIOGRAPHY

Vivek Bharambe received his Bachelor of Engineering degree with major in Electronics and Telecommunication Engineering from University of Mumbai, India in 2014. In Fall 2014, he joined the Master of Science program in Electrical Engineering at North Carolina State University. His research interests include RF/Microwave circuits, Electromagnetics, Antennas, EM simulations and 3D printing.

ACKNOWLEDGMENTS

I would like to express appreciation to my advisor, Dr. Jacob J. Adams for providing me an opportunity to work on this project and guiding me throughout the course of this research. Without his guidance and support, this thesis would not have been possible. I was introduced to a variety of new concepts and got insights on workings of academic research which led to my growth as a student, researcher and a professional.

I would also like to thank Dr. Michael Dickey for providing me insightful feedback from time to time thereby, improving the quality of my work. Regular interactions with him and his students were a constant source of new ideas that led to enhancement of my understanding of the technology I was working with.

A special thanks to the collaborators of the project, Dishit Parekh and Collin Ladd who helped me make this process possible with their can-do attitude, putting in late nights working in the lab, keeping updated with current research and helping me with the lab apparatus. Thank you to all the members of Antennas and Electromagnetics Lab research group at NC State University for providing me with advice to solve the issues I was facing and feedback on my work.

Lastly, I would like to thank my parents who have always been a source of motivation and support.

TABLE OF CONTENTS

LIST OF TABLES

LIST OF FIGURES

CHAPTER

1

INTRODUCTION

1.1. Additive Manufacturing

Additive Manufacturing (AM) is a printing technology which allows synthesis of 3D structures by layer over layer deposition of printing material. This technology has seen a rapid progress over the past decade on account of improvements in printing materials and deposition techniques. Enhancements in these technologies have also made the process simple and convenient. Today's 3D printers employing AM can easily transform a Computer Aided Design (CAD) model to a physical 3D print with a resolution of merely a few tens of microns. AM also has inherent advantages over the traditional techniques such as molding and casting as it reduces waste and has the potential to deliver high volume yields, maintaining low fabrication costs and high repeatability [1]. With the advent of multi-jet printing technology, it has also become possible to print very intricate and complex structures by depositing two or more materials with high precision. Additive Manufacturing technique is already being employed to solve a variety of niche problems in the fields of industrial manufacturing [2], medical implants [3], [4], Rapid Prototyping (RP) [5], [6] as well as arts and culture [2]. The various techniques used for Additive Manufacturing are explained in Chapter 2.

1.2. Additive Manufacturing in Electronics and RF

For a long time, the electronics manufacturing industry has focused on depositing metal traces onto planar substrates using methods such as lamination, laser printing, photolithography or chemical vapor phase deposition techniques. These methods have high set-up costs associated and some of them require development of expensive photo-sensitive masks for mass production. As a result, the retooling cost is higher as the design changes. While the traditional techniques have advantages in terms of speed and quantity, most of it can be attributed to the number of years of research dedicated towards perfecting these techniques.

For the semiconductor industry, complex processes to minimize fabrication costs are already primed but for manufacturing passive RF components such as waveguides, couplers, horns and antenna structures, the AM technology can provide a means for reducing costs, wastage and help rapid manufacturing of multifunctional, flexible and conformal devices. For example, a waveguide manufactured using traditional methodologies requires high-temperature molding, CNC machining, brazing and plating. With AM techniques, the same can be possible by simply 3D printing a CAD model of the waveguide and metallizing it with silver inks or electroless plating [7]. Using the commercial numerical solution EM solvers, it is possible to quickly find the frequency and time domain solutions of customized 3D EM CAD models within a short amount of time. Such customized 3D shapes can be readily printed with high resolution by employing AM.

In addition to building conventional designs, AM also provides a means to explore novel design potentials for enhancements in the performance of these devices. It adds degrees of freedom over the traditional planar/non-planar processes enabling construction of complex

3D structures. Such customized 3D structures can support current distributions not possible using planar/simple non-planar structures. This offers additional parameters in the hands of the designer enabling the development of 3D devices with an improved performance. For example, an electrically small 3D antenna developed by printing silver ink over a curved hemispherical surface was demonstrated to possess a higher bandwidth [8] than other compact planar structures. Thus, AM capabilities open up new prospects for rapid prototyping and bulk-manufacturing of such next generation high-performance antennas.

The scope of fabricating RF devices and antennas using most of the AM techniques is limited since they are adapted solely for printing polymeric parts. Embedding metals into the 3D printed geometries has for long been a challenge associated with the use of AM techniques for electronics. Most of the research in the field of AM has been to develop UV curable resins with superior mechanical performance since can provide a convenient and safer (as they have lower melting points) alternative to laser-based sintering techniques. While the AM technology is still in its developmental stages, it is early to expect patterning of metals with accuracy and convenience. There have been attempts to synthesize 3D structures using metal powders (Titanium, Aluminum, Stainless Steel) and a Laser system [9] but the use of this technology has been limited so far due to lower participation and high set-up costs. Alternatively, different methods such as electron beam evaporation, sputtering, electroforming, electroless plating and use of silver inks have been used to metalize the 3D printed polymeric geometries as discussed in Chapter 2 and Chapter 3. However, the limitation with the use of these techniques is that they cannot readily coat the internal surfaces of the parts.

Another interesting approach for constructing RF components for frequencies at the lower end of microwave range is to inject silver pastes in 3D printed molds and solidify them by evaporating the solvent. With proper design, this process can be used to metalize intricate 3D structures but this approach is restricted by the low conductivity of the paste [10]; thereby affecting the performance of the component. This challenge manifests due to the difficulty in achieving a high packing density of the paste inside the hollow cavities, thereby, limiting the conductivity to $2.8x10^5$ S/m even on repeated application. However, the approach can benefit from injecting alternate higher conductivity materials such as liquid metals.

1.3. Motivation for 3D Printed Liquid Metal Antennas

Mercury was initially investigated for constructing liquid metal antennas [11]. However, the research was later aborted owing to the high toxicity of the metal [12]. Eutectic Gallium Indium (EGaIn), an alloy of two metals, Gallium and Indium (75.5 and 24.5 wt. % of gallium and indium respectively), has recently caught attention amongst researchers on account of its low toxicity compared to Mercury [12], a high conductivity of $3.4x10^6$ S/m [12], high surface tension and its electro-chemical actuation abilities [13]. It has a higher conductivity as compared the silver paste ($2x10^6$ S/m) [14] and its liquid phase makes it an ideal candidate for rapid prototyping RF geometries. Antenna fabrication methodologies using liquid metals such as EGaIn and Galinstan have been earlier demonstrated for fabricating flexible and wearable antennas using a flexible polydimethylsiloxane (PDMS) substrate [15], [16]. This technique can be extended to enable metallization of precisely and rapidly built 3D

printed molds, allowing for high-fidelity conversion from CAD model to a prototype and high repeatability.

Moreover, the fluidic nature of liquid metals can also be exploited to create reconfigurable antennas [13], [17]. Reconfigurable antennas, as the name implies have an ability to change its fundamental properties such as operating frequency, pattern, polarization or bandwidths [18]. They have widespread applications when the antenna is expected to operate over a wide range of frequencies; for example, scanning of distant aircraft and projectiles for the military. The use of liquid metals to fabricate a frequency reconfigurable monopole antenna by altering the length of the antenna element in a capillary (microchannel) using electro-chemical actuation [13] and a polarization reconfigurable slot antenna fed with a Substrate Integrated Waveguide (SIW) structure [17] have been demonstrated in the past. Cosker et al. [19] used this approach to fabricate Planar Inverted-F Antenna using a flexible material NinjaFlex with Fused Deposition Modeling and injection of EGaIn into those channels.

The work presented here combines the advantages of both 3D printing (AM) technology and the liquid metal technology to fabricate antenna elements. Most of the prior research on constructing liquid metal devices focused on injection-based filling of microfluidic channels in combination with Printed Circuit Board type substrates/Copper based ground planes (or ground planes also composed of microfluidic structures itself [15]) as discussed earlier. This research proposes a procedure for use of liquid metals to metalize planar as well as non-planar, linear as well as curved hollow cavities using vacuum filling. The vacuum filling approach is well suited for filling arbitrary structures, quite adaptable to

microfluidic/planar/arbitrary-shaped geometries and can avoid large air-pockets in the metalized geometries if necessary precautions are taken (explained in Chapter 7). The proposed method explained in Chapter 5 can also be used to build flexible planar/arbitrary-shaped geometries using varied Additive Manufacturing techniques or elastomeric substrates. Later in Chapter 7, the issues faced during the implementation and the limitations of the process are highlighted. On further improvements to this technique, it can be utilized in the future to develop reconfigurable apertures by flowing the liquid phase metal alloys inside additively manufactured microchannels.

CHAPTER

2

ADDITIVE MANUFACTURING AND METALLIZATION TECHNIQUES

Additive Manufacturing (AM) technology, a widely-used approach for Rapid Prototyping (RP), was developed to realize three-dimensional prototypes by layer over layer deposition of polymers. The technology improved on account of research on alternate deposition techniques and formulation of a wide range of thermoplastics/photopolymers suitable for varied applications. While few techniques are still restricted by the materials that can be used, others are more versatile. It is essential to understand the technique to be used, its pros and cons in order to get a resolution and surface finish suitable for a particular application. Hence, the commonly used AM techniques are briefly explained below.

2.1. Additive Manufacturing Techniques

In this section, four of the most widely used AM techniques – Fused Deposition Modeling (FDM), Stereolithography (SLA), Selective Laser Sintering (SLS), PolyJet printing are discussed. A brief explanation and comparison of each of these techniques is provided to investigate the type of application suited for construction of 3D printed antennas.

2.1.1 Fused Deposition Modeling (FDM)

Fused Deposition Modeling (FDM), an Additive Manufacturing technology, is one of the most widely used printing technique for synthesizing 3D prints. FDM is a process of building structures layer by layer and fusing these layers to form a 3D structure. A typical FDM 3D printer uses a thermoplastic filament which is passed through a heating element that melts it to a semi-liquid state. As shown in Figure 2.1 (a), this molten plastic filament is then passed through an extruder and deposited accurately using a print head/extrusion head in the X-Y plane to form a layer. For the next layer, the extrusion head moves vertically upwards to deposit molten plastic on top of the previous X-Y layer. The motion of the print-head is accurately controlled by a Computer Aided Manufacturing (CAM) software package.

The advantage of Fused Deposition Modeling is that the materials are cheap and the technique does not require any chemical post-processing or additional UV curing [2]. This makes the process extremely attractive for applications where cost limitations are dominant. Since the process is based on depositing heated filament on top of the other, the technique has a poor resolution in the z-direction. The printed parts are susceptible to warping if not cured adequately and may require to manually sand-off the support materials. Alternatively, water-soluble support materials can be used for this process which makes the support removal procedure an easier task.

By far, FDM is the most common technique used to print substrates for fabricating 3D printed RF components and antennas. Most of this can be credited to an emergence of a variety of low-cost, high-precision FDM printers in the market in the past decade [6].

2.1.2 Stereolithography (SLA)

Stereolithography (SLA) is one of the earliest additive manufacturing technique which uses layer-on-layer deposition of UV-curable photopolymers to build a three-dimensional object. Instead of flooding the entire object with UV light for curing (as in case of PolyJet printing), a high precision selective curing mechanism employing a Laser/DLP-projector is used. The main components of the SLA machine are the resin-filled blade/coating system and a curing laser beam as can be seen in Figure 2.1 (b). The resin-filled blade sweeps across the print plate/platform surface and deposits a thin layer of photopolymer resin onto it. For this layer, the laser beam accurately traces the path as per the CAD model of the object to be printed and thus selectively cures the layer. This layer also fuses with the underlying layer during the curing process. As compared to FDM, SLA requires chemical post processing to eliminate the additional uncured residual resin from the sample [6] by way of a chemical bath. Processes for removal of support material and further curing of the printed part follow the chemical bath.

The pros of Stereolithography process are its speed, strength of the built object, surface finish [20] and its accuracy as compared to Fused Deposition Method. While the method is fairly simple, the requirement of a variety of solvents and the amount of post-processing make the process cumbersome and costly.

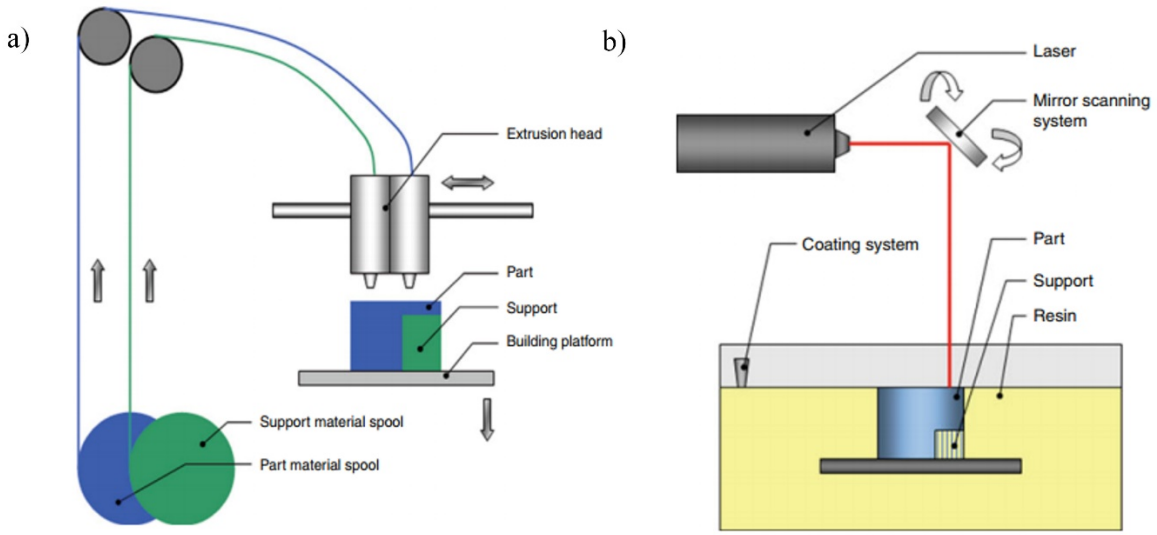

Figure 2.1 a) The working of a Fused Deposition Modelling technique which depends on extrusion of heated thermoplastics and b) The Stereolithography process which depends on selective curing of photopolymer using a Laser/Projector assembly [20].

2.1.3 Selective Laser Sintering(SLS)

Selective Laser Sintering (SLS) is also a selective curing based Additive Manufacturing process. The demarcation between Stereolithography and SLS method is that SLS method uses fine powder of materials, fused together by melting off the powder at high temperature attained using a carbon dioxide laser. Figure 2.2 (a) shows the roller that drops small particles of material onto the building platform that are selectively fused by the high-power laser. For this technique, the finest resolution achievable is defined by the size of the particles used for the synthesizing the print, thereby deciding the layer thickness. As the process involves melting-off small particles [2], the versatility of the process lies in its ability to print plastics, glass as well as metals. However, while printing metals, it is critical to avoid their oxidation and is achieved by filling an inert gas into the printing chamber. Use of polymer binders during

printing metals can strengthen the synthesized structure. SLS is a difficult process and handling a SLS machine requires a large amount of effort and preparation.

2.1.4 PolyJet Printing

PolyJet printing technology allows the use of two or more inkjet heads to print 3D structures. The technique was initially developed from traditional 2D inkjet printers that deposit tiny droplets of ink over a sheet of paper. PolyJet printers deposit small droplets of photopolymers and cure them with inexpensive UV flood lamps as shown in Figure 2.2 (b). Similar to other AM techniques, this process is also a layer-on-layer process. PolyJet printing is capable of synthesizing printed structures with high resolution and is known for its near paint-ready surface finish without the need for post-processing. This makes such prints ideal for depositing thin metal films using techniques such as electroless plating or sputtering. However, the disadvantage of this method is that the parts built using this technique are physically weaker than those by techniques such as SLS [2]. In addition, a chemical bath procedure is needed to remove the support material from the printed part, thereby increasing the operational costs and complexity compared to a simple FDM machine.

The type of printer used in developing 3D prints for this work is a PolyJet printer. It can print using up-to two materials, photopolymer and the support material. A fine resolution of up-to 29 μm can be achieved over the prints using this printer [21].

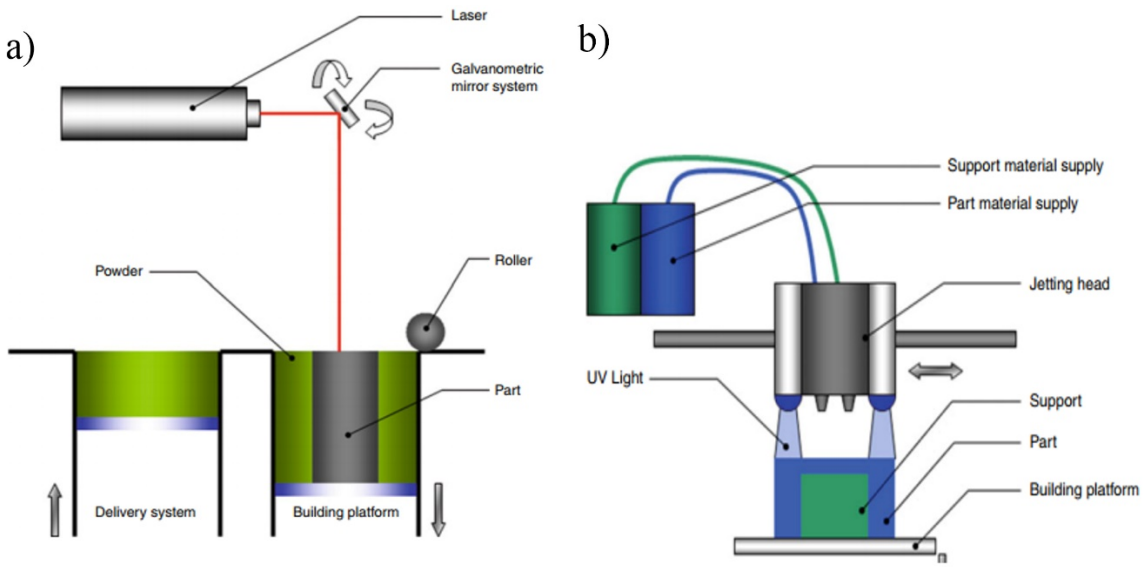

Figure 2.2 a) The working of a Selective Laser Sintering technique which depends on selective Laser based sintering of polymer/metal poweders and b) The PolyJet printing process which depends upon UV light flooding onto photopolymer inks extruded from jetting heads [20].

2.1.5 Comparison of AM Techniques

The Table 2.1 summarizes the different AM techniques and provides a comparison between them. This can be useful for selecting a technique suitable for particular application.

Table 2.1 Comparison of the different AM techniques.

	FDM	**SLA**	**SLS**	**PolyJet**
Material used	Thermoplastic filaments	UV-curable photopolymers	Metal, glass, plastic powders	UV-curable photopolymers
Material Deposition technique	Heated nozzle	Liquid phase resin blade	Roller-based powder deposition	Jetting of liquid polymers
Material phase change technique	Cooling	Curing by Selective Laser/Projector assembly	Partial melting by CO_2 laser	Curing by UV Flooding and cooling
Resolution of prints	Low	High	Low	High
Surface finish	Rough	Smooth	Rough and porous	Paint like finish
Operational difficulty	Low	Medium	High	Medium
Costs	Low	Medium	Very high	High
Popular materials	Thermoplastics: ABS, PLA, Nylon	Photopolymers: Ceramix, Accura 25, Accura 55 [22]	Metals: Aluminium alloys, Steel Others: Glass	Photopolymers: VisiJet M3 X, VisiJet M3 Crystal [15] and RGD5160, TangoBlack Plus FLX980 [23]

2.2 Metallization Techniques

In this section, the techniques used in the literature (discussed later) to create metalized surfaces for fabrication of RF components and devices are discussed.

2.2.1 Metal Deposition

This process involves depositing pure metal onto the additively manufactured surfaces. Particle bombardment processes such as sputtering, electron beam evaporation, electrochemical process such as electroplating and chemical deposition process such as electroless plating are used to deposit thin (a few microns thick) films of metal onto the thermoplastic/polymeric surfaces.

Sputtering and electron beam evaporation are both physical vapour deposition processes carried under vacuum. Both of these processes use high-velocity projectiles, gas ions and electron beam respectively to hit metal targets under vacuum to deposit thin films of the metal over a substrate. In the case of sputtering, this deposition takes place after ejection of surface atoms of the target onto the substrate, whereas in the case of electron beam evaporation, it takes place by condensation of vapors of the metal target over the substate.

Electrochemical deposition of metals onto the substrates is an alternative option to the techniques discussed above. Electroless plating is widely used in Printed Circuit Board industry for plating copper on the bare laminate by the virtue of a reaction between a reducing agent (mostly formaldehyde) and a copper salt [24]. The detailed process for the electroless copper plating is summarized using copper and formaldehyde/glyoxylic acid as a reducing agent in the book [24]. As can be seen in the Figure 2.3 the process takes place in a beaker

containing the plating solution at 60˚C. The plating solution is a mixture of the copper salt and the reducing agent. Films of an order of 3-5 microns can be achieved within an hour [24]. Electroplating is similar to electroless plating, the demarcation being the need of electricity for electroplating assembly compared to the auto-catalytic electroless plating process. Since it does not require a battery, electroless plating is a safer process and hence preferred over electroplating. While thin films of the order of few microns can be deposited using this technique, depositing thicker layers of high conductivity metals such as copper onto smooth surface prints can be challenging and lead to delamination and peeling effect [25].

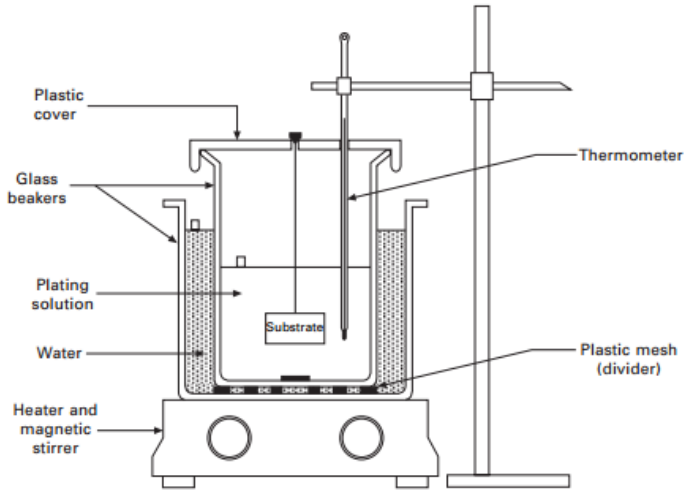

Figure 2.3 A diagram illustrating the process of electroless plating [24].

2.2.2 Conductive Inks and Pastes

The use of conductive inks to metalize the additively manufactured substrates requires formulation of low viscosity and high conductivity inks. Prior research has been dedicated towards the formulation of conductive silver inks [26] for applications such as writing conductive text, metal interconnects and developing 3D antennas [8]. Further enhancement in

this technique has lead to an increase in the conductivity of the silver inks to values > 10^6 S/m [26]. These silver inks can be used to coat the external surfaces of additively manufactured samples for metallization, however, dispensing them requires a precise rheology to coat/print on a surface. In addition, these inks require annealing at temperatures of a minimum of 90˚C [26], often ~550˚C [8], which can damage the geometries printed using materials with a low heat deformation temperature. Moreover, silver inks cannot readily coat the inner surfaces of printed parts.

Alternatively, silver suspension pastes can be used to metalize such hollow internal cavities [10]. A commercial product available in the market PELCO® uses 20 μm particles of silver in a silicate aqueous solution. However, it can be challenging to get high conductivity from such paste and packing them into hollow internal cavities.

2.2.3 Liquid Metals

Initial experiments with liquid metal antennas involved the use of Mercury. Mercury has a low viscosity and is a Newtonian fluid. It has a high surface tension and low adhesion to metal and dielectric surfaces. It has a melting point of -38.8˚C, a boiling point of 356.7˚C and does not oxidize easily. Although it has a lower conductivity of 1.02×10^6 S/m as compared to that of copper which is 5.96×10^7 S/m, the other inherent properties make it a good candidate for fabricating liquid metal antennas. However, owing to its toxicity [12], the metal can cause environmental and health issues which discourages any further work on mercury-based metallization.

Eutectic Gallium-Indium (EGaIn) is an electrically conductive fluidic alloy of two metals, 74.5% Ga and 25.5% In by weight. It has a conductivity of $3.4x10^6$ S/m [12] which is slightly higher than that of Mercury. Its melting point is 15.5˚C [12] and hence, a liquid at room temperatures. Cosker et al. [19] have demonstrated the viability of the use of injection of liquid metal to metalize 3D printed geometries. Liquid metal is more suited for fabricating flexible devices as unlike coated metals, they do not fracture on repeated stretching as a result of their liquid phase. This makes them an ideal candidate to construct flexible and reconfigurable antenna structures.

In summary, the advantages and disadvantages of the most widely used AM techniques were discussed. The suitability of different metallization techniques for varied 3D printing techniques was also discussed. For the design of small feature size geometries, high-resolution printing is essential. PolyJet printing was selected for this purpose. In the following chapters, the fabrication procedure using PolyJet printing and liquid metal filling will be proposed and its limitations will be highlighted.

CHAPTER

3

ADDITIVE MANUFACTURING OF RF COMPONENTS AND ANTENNAS

In this chapter, some of the examples of RF devices and components fabricated using additive manufacturing will be discussed. The method has been an active topic of research in the past decade. Since RF devices such as waveguides and horn antennas are still fabricated with metals by employing subtractive methodologies like milling and filing, the switch to additive manufacturing technologies in this field can help make these components inexpensive, light weight and accurate. In addition, batch printing of these components appears to be a better alternative than casting and molding of metals as changes in design would be convenient and would not involve significant retooling costs.

Radio Frequency components and antennas are geometry dependent devices. With additive manufacturing, geometries supporting different current distributions can be explored. However, before attempting construction of novel geometries using AM-based processes, it is necessary to examine the capability of the different approaches by studying these processes by building well analyzed, simple geometries. The examples of such simple RF devices and antennas fabricated using AM are widely available in literature and some of the versatile methods are mentioned in this chapter.

AM is not yet effective at patterning polymeric substrates and metals into one single printed structure. As a result, the 3D printing of different geometries is followed by a separate metalization process. A variety of approaches that use a combination of the additive manufacturing and metallization methods discussed earlier to build 3D functional RF components have been demonstrated in the literature.

One of the earlier attempt employing AM methodologies to design microwave frequency components was based on the synthesis of corrugated horn antenna using high-resolution Stereolithography (SLA) technique. Timbie et al. [27] used electroless deposition of 1 μm thick Ni layer followed by 5 μm thick Cu layer to get good conductivity for the horn antennas operating in W-band frequencies of 75-110 GHz. The corrugated horn antenna shown in Figure 3.1 (a) has main beam patterns nearly identical to that achieved using electroforming. Geterud et al. also presented additively manufactured light weight X-band waveguides fabricated using extrusion of a thermoplastic polymer, Acrylonitrile Butadiene Styrene (ABS) and SLA printing. It was metalized using electroless plating of up-to 4-5 μm thick copper onto the surface [7] and the loss per unit length of the fabricated waveguide was less than 0.035 dB/cm. The advantage is that the waveguides designed using these procedures, as shown in Figure 3.1 (b) have low weight and can be easy to manufacture. However, it can be difficult and time-consuming to deposit thicker layers (for lower resistance) using plating over plastic technique that restricts its use for lower band of microwave frequency range.

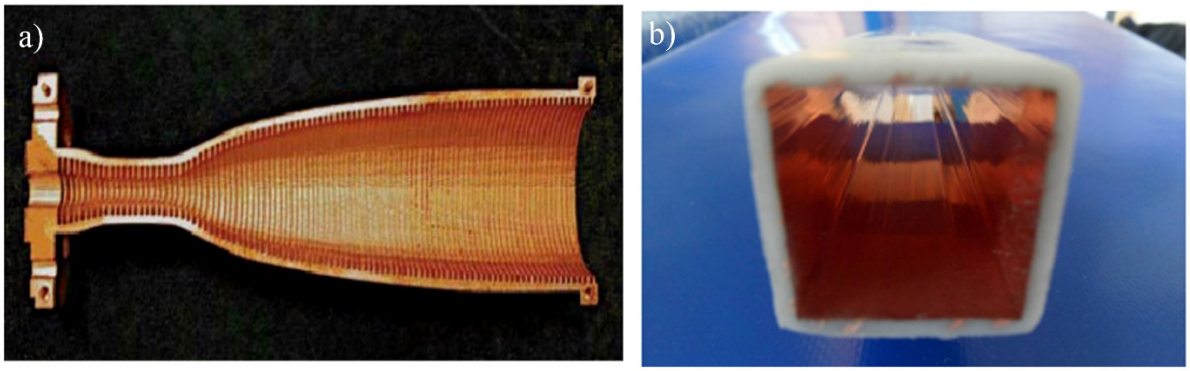

Figure 3.1 a) The corrugated W-band waveguide fabricated using electroless plating [27] and b) The X-band waveguide fabricated using ABS extrusion and electroless plating of copper on the inner surface [7].

Wu et al. [28] proposed a fabrication methodolgy that works on selective metallization of the surface of additively manufactured conformal structure as shown in Figure 3.2. A conformal mask is also built using additive manufacturing by projecting the surface to be metalized. A variety of methods such as electron beam lithography, sputtering and electroforming were tested to deposit copper to fabricate the array. This work captures the true sense of being able to manufacture devices that have the ability to conform to lots of complex surfaces.

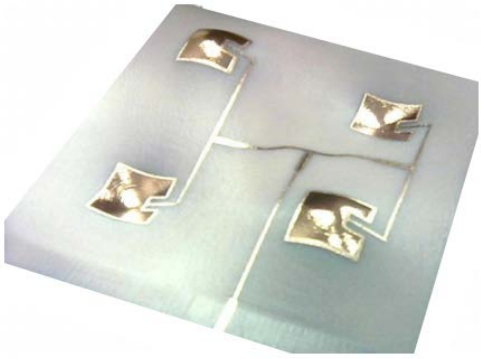

Figure 3.2 The additively manufactured conformal substrate for patch array metalized using an electron beam [8].

However, while it is easier to coat external surfaces using this technique, internal surfaces of the 3D printed geometries are difficult unless they are printed as a cross section cut and assembled later as demonstrated for fabrication of the X-band filter [29].

An alternative to plating over plastic approach is to use conductive inks to metalize the structures. Inkjet printing of conductive inks [30] to develop RFID tags on a Polyethylene Terephthalate (PET) film was attempted, but its scope is still limited to planar geometries. Bryan Willis [31] demonstrated the rapid prototyping of certain types of 3D devices with this metallization technique. With silver inks allowing metallization of 3D geometries, research was also directed towards printing of silver inks to form conformal antenna structures [8] onto hemispherically curved surfaces as shown in Figure 3.3. Such geometries can help in increasing the bandwidth of the antennas while maintaining a compact form-factor. However, the dispensing of these inks require a precise rheology followed by annealing at around 550 ˚C (minimum of 90 ˚C [26]) to improve the conductivity. Such a high-temperature treatment can destroy the 3D printed parts built using AM techniques and alternatives need to be explored.

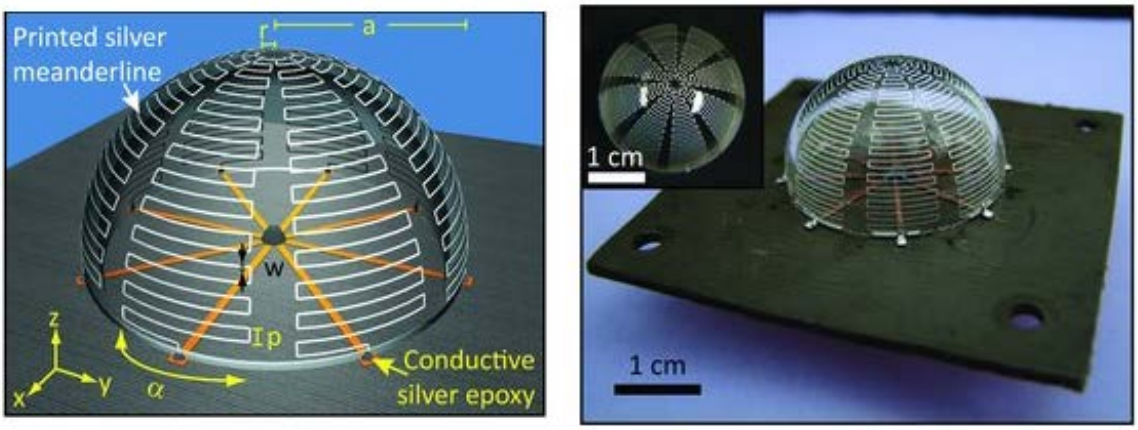

Figure 3.3 An illustration of silver ink conformal printing technique on concave/convex surfaces [8].

For the synthesis of 3D printed devices with embedded metallization, the ultrasonic wire-mesh embedding technique can be used. Liang et al. [32] used this technique to design and fabricate a multilayer microstrip line structure along with vertical transitions using Fused Deposition Modeling technique. The measured insertion loss for a 90 mm long transmission line with one vertical transition as shown in Figure 3.4 was as low as 2 dB for frequencies below 6 GHz. The material used in this process was ABS which is one of the most commonly used FDM thermoplastic and the wire-mesh structure was embedded into it. This makes the printer capable of both – printing the acrylic substrate as well as metalizing the structure. A large number of applications such as building soft sensors, 3D antenna structures can be possible using this approach. Since the printer uses FDM, the resolution of prints can be a limiting factor for the performance of the fabricated devices at higher frequencies.

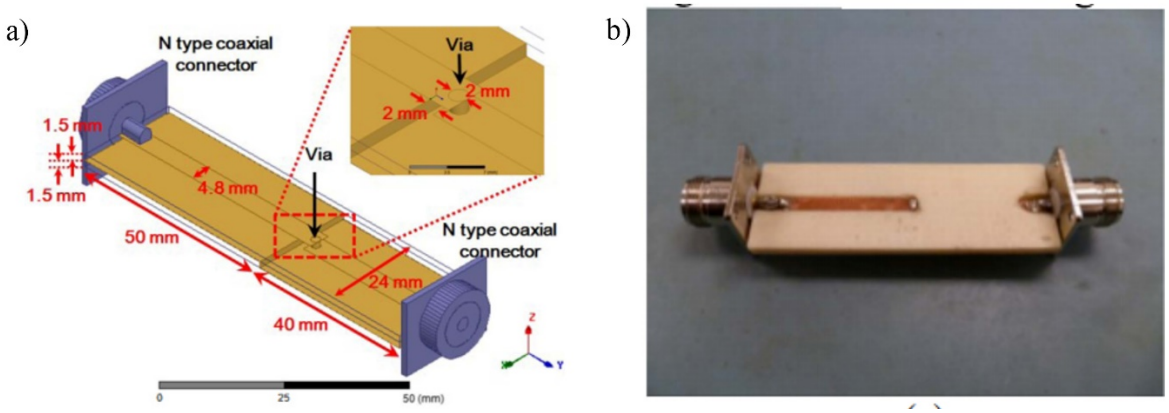

Figure 3.4 a) The planar transmission line with one vertical transition built using FDM [32] and b) The actual fabricated model of the transmission line built using wire mesh embedding [32].

An easy and convenient approach to develop non-planar and true 3D RF components involves use of a silver-suspension paste. Wu et al. [10] used PolyJet printing to develop 3D strutctures with hollow cavities. These hollow cavities as shown in Figure 3.5 (a) were

metalized later by injecting a silver suspension paste to fabricate basic components such as resistors, inductors and capacitors. While the performance of these components looks promising, the Q of the inductors and capacitors are low due to the poor conductivity of the silver paste. This approach can benefit from alternative paste/liquid metal injection as demonstrated by Cosker et al. [33] in fabrication of Planar Inverted F Antennas using a flexible material NinjaFlex and liquid metal injection in microchannels as shown in Figure 3.5 (b).

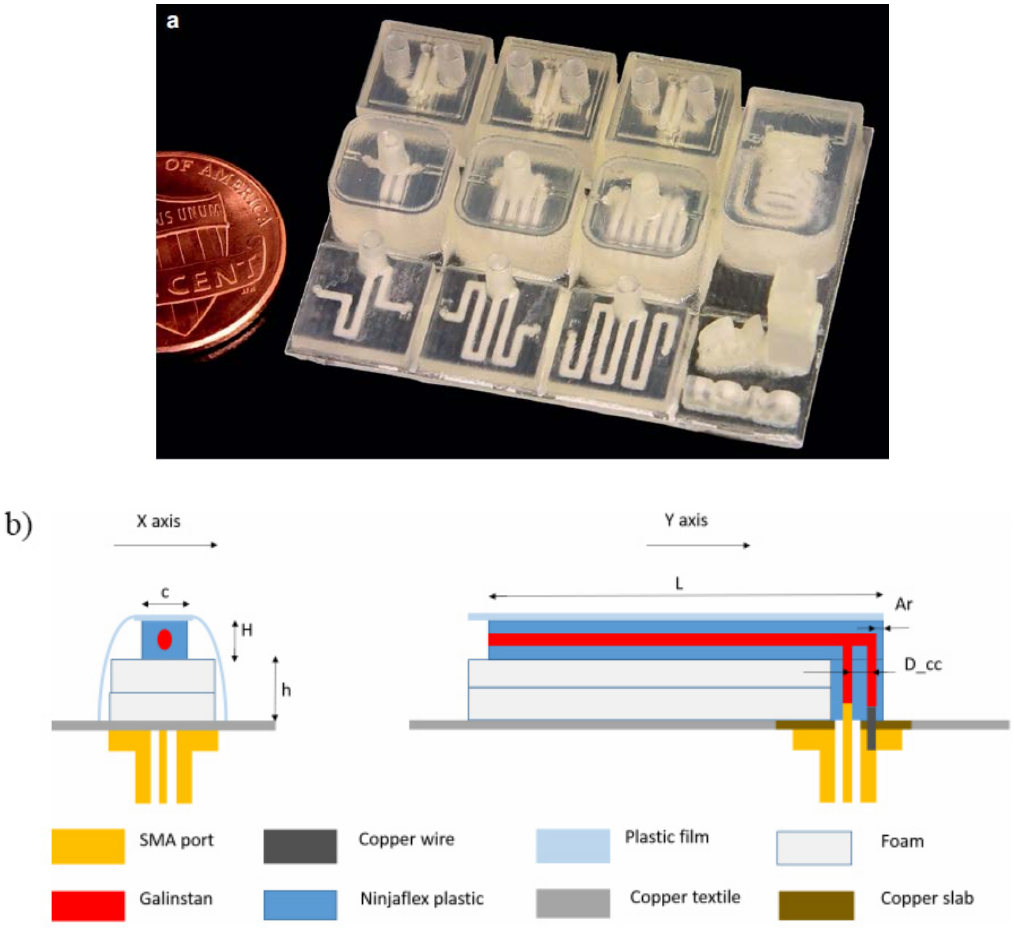

Figure 3.5 a) The additively manufactured hollow cavities printed by PolyJet printing to be metalized by silver paste [10] and b) The 3D printed and liquid metal filled flexible PIFA [33].

Gallium alloys have higher conductivity than silver suspension pastes and do not undergo solidification at room temperatures, making them an ideal option for filling 3D printed geometries, if the leakage issues (explained later) are resolved.

Not every approach is ideal for all type of applications. The primary criteria for selection of an approach should be the frequency of interest, the sturdiness, the utility of the fabricated structure should be taken into consideration. The frequency will put a limitation on the resolution of the prints essential while the sturdiness requirement will define the AM/metallization approach best suited for the application. Hence, a careful evaluation of each of the technique is needed. In the next chapters, we will be proposing an extension to the existing liquid metal antenna fabrication process by using vacuum-based filling approach instead of the conventional injection-based filling of microchannels to give the flexibility to incorporate planar as well as non-planar geometries into the design.

CHAPTER

4

PROPERTIES OF THE MATERIALS

The available 3D printer ProJet 3500HDMax supports a wide range of proprietary materials, VisiJet M3 Crystal, VisiJet M3 Navy, VisiJet M3 X, VisiJet M3 Black, VisiJet M3 Proplast, VisiJet M3 Techplast, VisiJet M3 Procast [21]. These materials vary in their physical and chemical properties. The physical properties are important as they determine the build quality, surface finish and sturdiness of the model. Knowledge about properties such as melting point, density, viscosity can help develop an optimum process for fabrication. In addition, the complex electrical permittivity of these materials also needs to be determined so as to design electromagnetic devices using them.

In this chapter, the physical properties of the support material and criteria of selection of a printing material will be discussed based on its physical properties. Since no previous documentation of the electrical characterization of the 3D printing acrylic material was available, a resonant cavity was built to measure the complex permittivity of one of the material, VisiJet M3 Crystal.

4.1.Physical Properties of the 3D Printing Materials

In this section, the physical properties of the materials are discussed. Along with different additive manufacturing techniques as discussed in Chapter 2, the materials play an integral role in defining the quality, resolution and the strength of the print. Efforts have been made to develop a variety of materials that have desirable qualities such as low melting point, UV curability and high mechanical strength. Of these options stated above, VisiJet M3 Crystal was used to fabricate the antennas on account of its high flexibility, high strength, relatively lower distortion and natural color appearance [21]. It has a low melting point in the range of 55˚C – 65˚C that makes it easy to extrude from the nozzles of the printer and also has a relatively higher heat distortion temperature of 55 ˚C once cured [21]. It has a density of 1.1g/cm^3 [21] and is slightly soluble in water. It is a tough plastic and only undergoes an elongation of about 6.8% [21] before experiencing a break.

The support material used by the printer to print hollow geometries is VisiJet S300. Some of its desirable properties are the ability to hold the structure, high dissolvability, low melting temperature and easy elimination. VisiJet S300 is a white wax-like meltaway substance with a melting point of 60˚C [21]. Thus, the printing material VisiJet M3 Crystal will undergo less distortion during the process of dissolution of the supports.

4.2. Characterization of Complex Permittivity

To enable antenna designs, it is necessary to characterize the complex electrical permittivity of the material in which the antenna is embedded. It is a function of the frequency

of the wave incident on the material and the dispersion equation of the material expressed as [34]

$$\varepsilon = \varepsilon' - j\varepsilon'' \tag{4.1}$$

The real part of the electrical permittivity ε', also known as the dielectric constant of the medium is related to the electric susceptibility of the medium and is a measure of the ability of the material to undergo polarization on the incidence of an electric field. The effective electric loss tangent or simply called the loss tangent $(\tan\delta)$ is a measure of the losses experienced in the media as a result of damping of the motion of negative charges on excitation by a harmonic electric field with angular frequency ω [34] and is expressed as

$$\tan\delta = \frac{\varepsilon'}{\varepsilon''} \tag{4.2}$$

The characterization of the complex permittivity can be done by using a transmission line method [35], resonant cavity method [35], capacitance method [35], the ring resonator method [36] or by the waveguide method [37]. The parallel plate capacitor method is widely used to characterize the permittivity for a low-frequency range, where the inductive parasitics do not play a dominant role. The ring resonator method, the cavity method and the waveguide method are most commonly used for high-frequency characterization. While the waveguide method uses complex scattering and reflection theory for characterizing the properties of the material, the ring resonator and the cavity method depend on measurements of the shift in the resonance frequencies to determine these properties. For permittivity characterization of a 3D printing resin, the cavity resonator method offers a good compromise between accuracy and simplicity as it is easy to 3D print blocks of the material to be inserted into the cavity for

measurements. An additional merit of this method is that it has a high repeatability and consistency once the cavity has been fabricated and tested. For this reason, the permittivity characterization was performed using this method. A cylindrical resonant cavity of radius 'a' cm and height 'h' cm $(h \approx a)$ was constructed as shown in Figure 4.1.

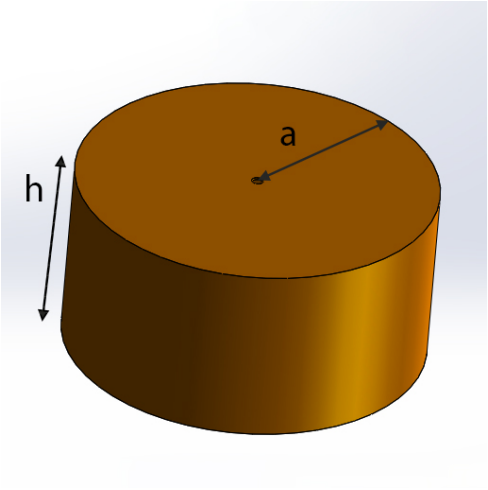

Figure 4.1 An illustration of the dimensions of the resonant cavity

The dimensions and the feed position determine the modes which can be excited in the cavity and their respective resonant frequencies. The cavity was fed with a probe from the top surface. The frequency of resonance for the different modes of the cavity, TM_{mnp} can be calculated by the formula [34]

$$f_{TM_{mnp}} = \frac{1}{2\pi\sqrt{\mu\varepsilon}}\sqrt{\left(\frac{\chi_{mn}}{a}\right)^2 + \left(\frac{p\pi}{h}\right)^2} \tag{4.3}$$

The term χ_{mn} is the n^{th} zero of the Bessel function of the first kind of the order m. The lowest value of the zero of this function is when $m = 0$ and $n = 1$. The TM_{01p} modes can be excited into the cylindrical cavity by means of a probe feeding from the top. Thus, the

fundamental resonance of the cavity should be when $p = 0$ that is the TM_{010} resonance whose frequency for an air-filled cavity $(\varepsilon_r' = 1)$ can be calculated from equation 4.3 as

$$f_{TM_{010}} = \frac{1}{2\pi\sqrt{\mu\varepsilon}} \times \left(\frac{2.4049}{a}\right) \tag{4.4}$$

Two cylindrical cavities were built with the radius as 3.8 cm and 1.1 cm to characterize the permittivity for frequencies around 1.5 GHz and 6 GHz (on introduction of printing material) respectively. These two fabricated cavities are shown in Figure 4.2 (a).

Full-wave simulations of the setup were carried out using HFSS, Ansys Inc. and the precise probe length required to excite the TM_{010} mode was found out. The simulations also verified the frequency of resonance for this mode as shown in Table 4.1.

Table 4.1 The comparison of resonant frequencies of the air-filled cylindrical cavities by analytical calculations, simulations and measurements. The measured and simulated resonant frequency was found by observing the frequency at which the input resistance peaks.

No.	Radius of cavity (cm)	Analytical (GHz)	Simulated (GHz)	Measured (GHz)
Cavity1	3.825	2.99	2.99	2.982
Cavity2	1.1	10.43	10.41	10.44

Since VisiJet M3 Crystal was selected for printing of the antenna geometries, and the co-printed VisiJet S300 was simply a meltaway material, only the characterization of electrical permittivity of VisiJet M3 Crystal was essential. Its determination was done by taking two measurements, one with air as a medium and other with VisiJet M3 Crystal as the dielectric medium inside the cavity. As almost the entire medium inside the cavity was replaced, the shift

in resonances for the mode was inversely proportional to the square root of the real part of the permittivity.

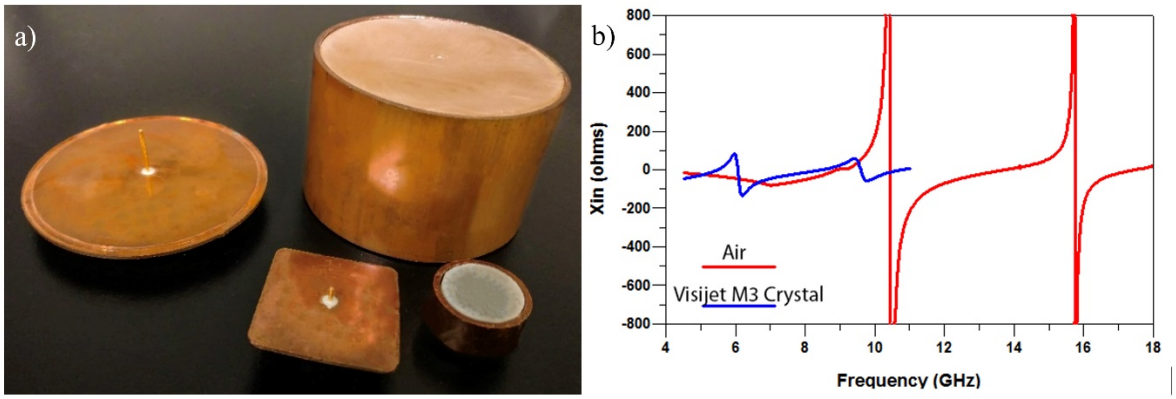

Figure 4.2 a) The fabricated cylindrical resonant cavities with radius 1.1 cm (front) and 3.825 cm (back). **b)** The measured resonance of the air-filled cavity (red) showing a resonant frequency for the TM_{010} mode as 10.44 GHz and TM_{011} mode as 15.85 GHz. The measured resonance of VisiJet M3 Crystal filled cavity (blue) for TM_{010} mode as 6.068 GHz and for TM_{011} mode as 9.6 GHz.

From the Table 4.2, it can be observed that the real component of the permittivity of VisiJet M3 crystal is fairly constant over a range of frequency of 1.5 GHz to 6 GHz. An estimate of 3 was selected for ε_r' to account for the air gaps present between the block and the cavity walls during the VisiJet M3 Crystal measurements.

Table 4.2 The comparison of the measured dielectric constant of the VisiJet M3 Crystal samples (sample radii reduced to fit into cavity)

		Sample1	Sample2	Sample3
Radius of samples (a) cm		1.09	1.09	3.8
Resonant frequency $f_{TM_{010}}$ (GHz) (max(real(Z11)))	Air filled cavity	10.44	10.44	2.98
	VisiJet M3 Crystal filled cavity	6.068	6.072	1.73
Calculated ε_r'		2.96	2.96	2.96

The loss tangent of the material $(\tan\delta)$ was determined by calculating the Q by taking partial frequency derivative of the input impedance of the cavity as shown in [38]

$$Qz(\omega_0) = \frac{\omega_0}{2R(\omega_0)}\sqrt{\left(\frac{\delta R(\omega_0)}{\delta\omega_0}\right)^2 + \left(\frac{\delta X(\omega_0)}{\delta\omega_0} + \frac{X(\omega_0)}{\omega_0}\right)^2} \tag{4.5}$$

The equation 4.5 provides a way of calculating the Q of the cavity for both the cases, the air-filled cavity and the dielectric media filled cavity. The Q of the cavity filled with air as a medium will only have losses due to resistance of cavity walls and losses experienced in the SMA connector associated with it. These quantities can be effectively coupled into the term Q of the cavity or 'Q_{cavity}'. Once the dielectric media is introduced into the cavity, an additional factor, the losses in this dielectric media will be responsible for reducing the Q. This Q is called the loaded Q or simply the total Q of the cavity, denoted as 'Q_{total}'.

Thus, with these two measurements, the loss tangent can be calculated using the formula,

$$\tan\delta = \frac{1}{Q_{diel}} = \frac{1}{Q_{total}} - \frac{1}{Q_{cavity}} \tag{4.6}$$

After repeating the measurements over two different samples the estimated value of $\varepsilon_r^{'}$ was fixed as 3 and that for $\tan\delta$ was taken as 0.045 as a close approximation to the average values at a frequency of 6 GHz.

Table 4.3 The comparison of the loss tangent of the three samples

	Q_{total}	Q_{cavity}	$\tan\delta$
Sample1	21.68	314	0.043
Sample2	18.64	314	0.050
Sample3	19.07	2700	0.052

Since the electrical permittivity of the printing material is characterized, antenna designs can be developed by using these values. These values contrast with the permittivity characterization of a similar material, VisiJet EX 200 [10] carried out using a capacitance based measurement technique available in the literature. However, antennas designed using these values in Chapter 6 demonstrate a close alignment with the measured results as discussed later.

CHAPTER

5

FABRICATION PROCEDURE

In this chapter, the proposed procedure to fabricate liquid metal antennas is introduced. The basic idea of the procedure is to use the available PolyJet printer to build the geometries using two materials, the printing material and the support material. The support material holds up the shape of the structure throughout the printing process. This arrangement enables fabrication of hollow cavities. Once the structure is cured by UV light flooding, the support material can be dissolved and flushed to create hollow cavities in the print which can be filled with liquid metals later using vacuum based filling or pressure driven filling. The distinct steps for fabricating the liquid metal antennas are depicted using a flow-chart as shown in Figure 5.1 (a) and schematic in Figure 5.2 provides graphical illustrations of the procedure.

5.1. 3D Printing of Antenna Geometries

The 3D printer used in the process of fabrication of the structure was ProJet 3500 HDMax printer. It is a PolyJet printer which allows the use of two different materials for building a 3D print and has a layer resolution of up-to 29 μm in UHD mode [21]. One of the heated jet nozzle ejects a UV curable molten polymer VisiJet M3 Crystal and deposits droplets

of the material stacked upon and besides each other. The other nozzle ejects the support material VisiJet S300 as needed. This material is used to provide mechanical support during the printing process. It is mostly a sacrificial wax like material that can be melted and flushed subsequently to create the hollow cavities in the designed geometries.

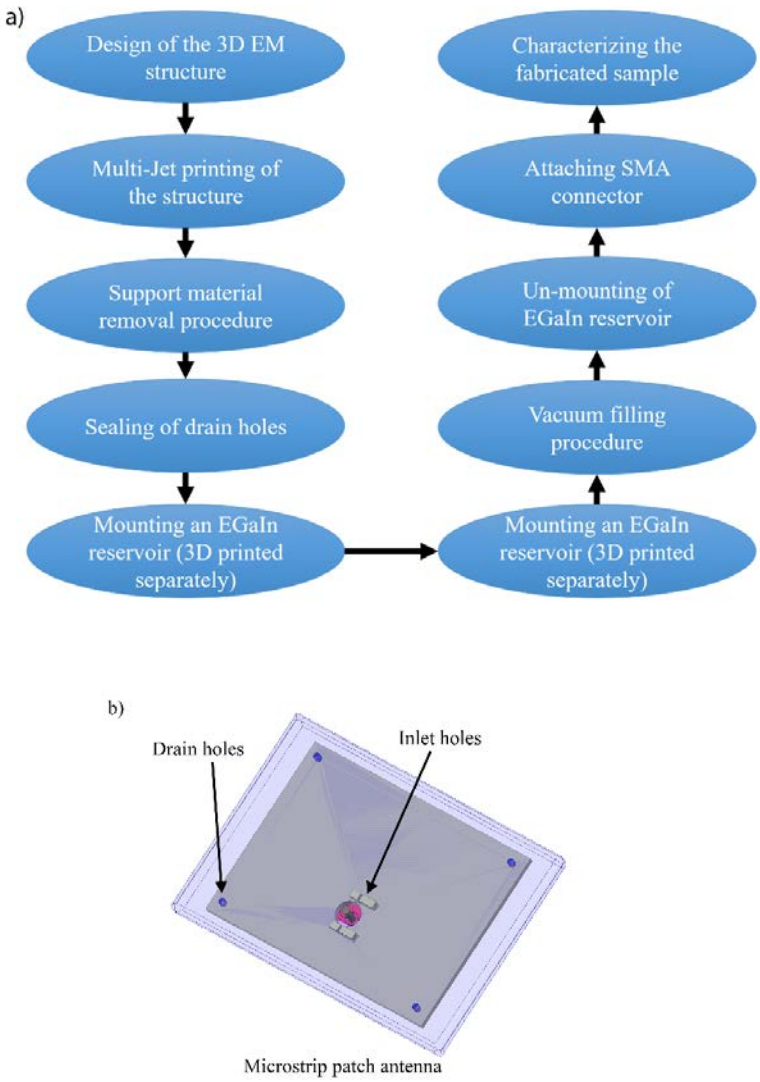

Figure 5.1 a) The process flow-chart for fabricating liquid metal filled 3D printed antennas and b) The antenna structure to be printed is designed using an EM simulation tool with the correct material properties assigned and 3D printed.

As can be seen in Figure 5.1 (b), the antenna geometries with EGaIn inlet holes and small drain holes for support material are designed using HFSS, Ansys Inc. and later converted to a CAD part file for printing. The printer uses 618 nozzles for its 3D inkjet printing technique using UV curable printing and support material mentioned earlier to create these prints onto a printpad. Once the structure is printed as shown in Figure 5.2 (a), it is required to place the sample in warm EZRinse-C solution supplied by 3DSystems in a sonicator to melt and eliminate the support material. M3 Crystal printed components may undergo slight deformation in shape as the temperature goes above 56˚C [21]. However, as the melting temperature of the support material VisiJet S300 is 60 ˚C [21], it is critical to maintain temperature of the solution close to this value to ensure minimum distortion in shape. Once the support material is dissolved, the sample is washed thoroughly with warm water to remove the residual dissolved wax. The water is then allowed to drain off the sample. Drain holes added to the design at the edges during the design process simplify this process of removing the maximum amount of support material and water. Any trace reminiscent of the support materials or water is then eliminated by placed the sample in a vacuum oven at 56˚C for a few hours. Once the wax supports have been cleared, outlet holes are sealed using a drop of UV curable thioester (Norland Optical Adhesive - NOA63) glue over them as shown in Figure 5.2 (b). It is then rapidly cured with UV light to prevent it from entering the hollow cavities to be metalized later.

5.2. Vacuum Filling of Liquid Metals into Hollow Cavities

Once the outlet holes are properly sealed, a detachable liquid metal reservoir (3D printed separately) is mounted onto the structure and sealed for the vacuum-filling process. The Figure 5.2 (a) demonstrates the antenna geometry with the attached reservoir filled with the volume of liquid metal required to fill the antenna and an additional 30%-50% to avoid air from re-entering the cavities towards the end of the process as shown in Figure 5.2 (c). This sample, along with the reservoir is kept in a vacuum chamber at a pressure of -30inch Hg relative to the atmospheric pressure for ~30 minutes. After this time, the entire vacuum chamber is rapidly brought to atmospheric pressure. As shown in Figure 5.2 (c), this forces the liquid metal into the hollow cavities of the structure while maintaining an air-lock mechanism on account of the additional volume of EGaIn added earlier. As can be seen in Figure 5.2 (c), the pressure outside the sample is the atmospheric pressure (P_{atm}) while that inside the hollow cavities is still the vacuum pressure (P_{vac}). Due to this pressure differential, the atmospheric pressure drives the liquid metal into the cavities. Once the cavities are filled with liquid metal, the reservoir is then detached as shown in Figure 5.2 (d) and RF connector is sealed using an optically curable sealing glue (NOA-63) at the inlet of the structure as shown in Figure 5.2 (e).

One of the challenges of this process is to analyze the adequate pressure required for complete filling of liquid metal into the cavities when smaller feature sizes are concerned and depends a lot on the type of geometry. With lower dimensions, the amount of pressure required to fill the cavities will be higher. For some of the features of the designed antennas, channels of dimensions as small as 500 μm were tested. Partial support material removal and high flow

resistance are two of the challenges faced while trying to construct designs with even smaller channel dimensions.

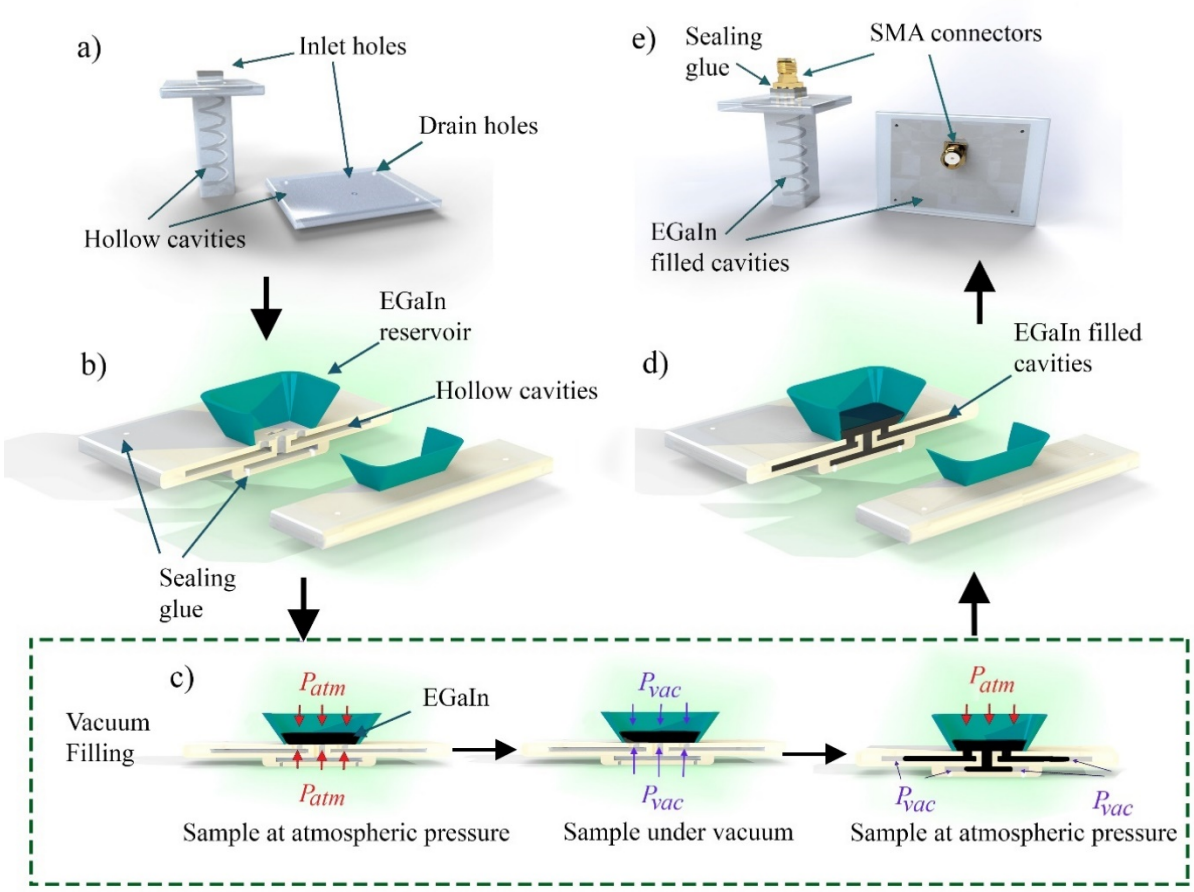

Figure 5.2 a) The 3D printed acrylic structures with embedded hollow cavities formed as a result of support material removal, b) – d) The illustration uses cross-sectional cut of patch antenna to demonstrate the vacuum-based liquid metal filling procedure and e) A SMA connector interfaced to liquid metal seals the inlet of the hollow cavities.

Even for relatively large feature sizes, it is difficult to correctly determine whether the cavities are filled entirely. While flow rate or volumetric analysis can be done for evaluation, it will still be limited by the accuracy of these measurements. A Computer Tomography (CT)

scan of the filled patch sample can be used to detect visible tiny voids in the ground/patch planes but it cannot be used to determine the exact filling efficiency. Electrical performance and comparison to a void-free simulation model of the device can be a preliminary step to evaluate this. Figure 5.3 illustrates the results of the scan of an early patch antenna prototype indicating the presence of the voids.

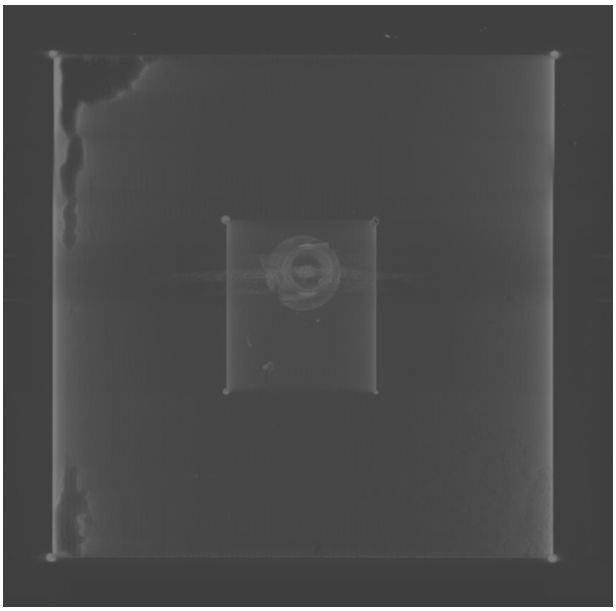

Figure 5.3 The CT scan of the patch antenna indicating presence of voids filled with air in the ground plane.

In summary, the vacuum filling approach is proposed and it needs to be tested as a viable means for metalizing planar and non-planar geometries by developing different antenna designs. On testing over a wide variety of geometries, an idea about the challenges and limitations of the process was obtained and will be discussed in Chapter 7.

CHAPTER

6

ANTENNA DESIGN, MEASUREMENTS AND DISCUSSION

The previous chapter introduced the proposed procedure to fabricate antenna geometries with embedded liquid metals. In this chapter, certain antenna geometries were selected with the intention of testing this procedure. The motivation of selection of each type of geometry, its design procedure using the materials discussed above and the observed results are presented.

6.1. Microstrip Patch Antenna

In this section, a preliminary investigation of the viability of liquid metal filling approach for additively manufactured antennas is provided by utilizing a simple microstrip patch geometry. Since the substrate is additively manufactured as opposed to using a traditionally available Printed Circuit Board type of substrate, assumptions made to justify deviation of values from analytical calculations are provided.

6.1.1 Motivation for Fabrication of Microstrip Patch Antenna

The simple construction and easy feeding mechanism for a planar microstrip patch antenna was the biggest motivation to fabricate this type of geometry. Furthermore, its

fabrication mandates a thorough cleaning of the support material and metallization of two hollow planar structures, the patch element cavity and the ground plane cavity. Thus, vacuum filling procedure could be effectively verified for metallization of such planar cavities as opposed to the widely investigated microfluidic channels.

6.1.2 Background

Microstrip patch antennas find application in fields ranging from military to commercial products. These low-profile antennas are advantageous owing to their planar geometry which makes them light-weight, cost-efficient and fairly inexpensive.

Microstrip patch antenna is a radiating structure which consists of a thin metallic strip placed at a height (h) above a metallic ground plane. The metallic strip can be square, rectangular, circular, or any other arbitrary shape. Of these, the more popular rectangular strip having length L and width W placed at a height h above the ground plane in a medium with dielectric constant ε_r' is demonstrated in Figure 6.1. These geometries have been exploited to create conformal and flexible antennas for nonplanar surfaces as well [15], [39]. In addition, adding slots on the patch can help create a circularly polarized pattern instead of a linearly polarized one [40]. Similarly, a variety of feeding techniques such as coaxial feed, proximity coupling, microstrip feed, proximity coupling can be used to excite a patch antenna. The feed type and location can determine the modes that can be excited. The coaxial type of feeding shown in Figure 6.1 is used to design the patch antenna discussed later.

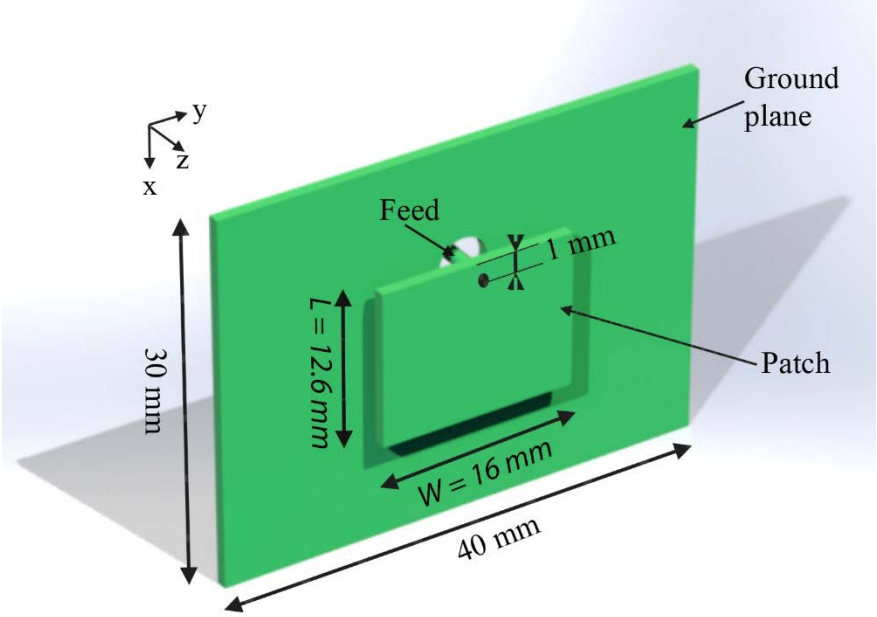

Figure 6.1 Structure and dimensions of the designed microstrip patch antenna.

6.1.3 Design Procedure

Transmission line model [41] is one of the easiest ways to design and analyze a microstrip patch antenna. This model indicates that the patch would be resonant when the length (L_1) of the patch designed for a substrate with dielectric constant (ε_r') is related to the free space wavelength (λ) of the wave at the design resonance frequency (f_r) [41] as

$$L_1 = \frac{\lambda}{2\sqrt{\varepsilon_r'}} \tag{6.1}$$

It is also important to consider the effect of fringing electric fields originating from the patch and ending at the ground plane. This effect results in an apparent elongation of both of the dimensions of the rectangular strip. As a result, the resonance can be achieved with a strip length lower than that calculated using the equation 6.1. For a Printed Circuit Board (PCB)

type of substrate, this apparent elongation (ΔL) is dependent on the width (W) of the patch and the height of the substrate (h) and can be expressed using the formula [41],

$$\Delta L = 0.412h\frac{\left(\varepsilon_{reff}+0.3\right)\left(\frac{W}{h}+0.264\right)}{\left(\varepsilon_{reff}-0.258\right)\left(\frac{W}{h}+0.8\right)} \tag{6.2}$$

Here the effective dielectric constant of the media ε_{reff} is characterized for a PCB type of substrate (Rogers Duroid, FR4) which accounts for the electric field lines traveling through air and the substrate. It should be noted that this elongation occurs at all the four edges of the patch. Hence the effective resonant length (L) of the patch can be calculated by subtracting this elongation (ΔL) from the length (L_1) found out earlier using equation 6.1 as,

$$L = L_1 - 2(\Delta L) \tag{6.3}$$

While such substrates have a substrate-air interface along the plane of the patch, the same is not true for our case; wherein the liquid metals are enclosed in cavities surrounded by dielectric media. However, these calculations provide a good estimate for the values to be used for a full wave 3D EM simulation. The calculated value for L_1 is 14.4 mm for a microstrip patch antenna operating at 6 GHz embedded inside VisiJet M3 Crystal with a dielectric constant of 3. This provides an initial estimate that the effective resonant length (L) should be lower than 14.4 mm and will be determined using full-wave EM simulations.

The width (W) of the patch antenna plays an important role in determining the directivity of the patch antenna and the its input resistance. The larger the width, the higher is the directivity and the lower the resistance. Hence, the value of the width would depend upon the input resistance and the directivity requirement. When $W > L > h$, the TM_{010} mode of

resonance can be excited by using the feed location as shown in Figure 6.1. The width of the patch (W_1) required to achieve an impedance close to 50 Ω and a high directivity can be calculated as [41]

$$W_1 = \frac{1}{2\pi\sqrt{\mu_0\varepsilon_0}}\sqrt{\frac{2}{\varepsilon_r + 1}} \tag{6.3}$$

The actual width (W) would be lower than this value on account of fringing fields as described earlier. For filling the patch geometry with liquid metal, a direct feeding co-axial structure was selected. The inner conductor of this structure directly opened into the patch geometry and the outer conductor opened into the ground plane and this arrangement can provide a path for liquid metal into these cavities (illustrated in Figure 5.2 (b). Using a direct feed arrangement, the input impedance of the antenna structure can be matched to the feed impedance of 50 Ω by using an offset in the location of the feed from the edge of the patch as shown in Figure 6.1.

With these calculations, a full-wave simulation of the entire geometry was set up. The length and width of the ground plane were set as 30 mm and 40 mm respectively. To ensure proper filling of the ground and patch planar cavities, a thickness of 1 mm for both these cavities was used and the separation between them was also kept as 1 mm. The width (W) of the patch was taken from the calculation from equation 6.3 as 16 mm and the length (L) of 12.6 mm was determined for a resonant frequency of 5.98 GHz. To match the antenna input impedance to 50 Ω, an offset of 1 mm from the edge of the patch was determined using the simulations. The dimensions and orientation of the geometry is illustrated in Figure 6.1.

The actual printed sample with the cavities for ground plane, patch and the co-axial feed generated by removal of the sacrificial support material and flushing it is shown in Figure 6.2 (a) and with the sealed SMA connector in Figure 6.2 (b).

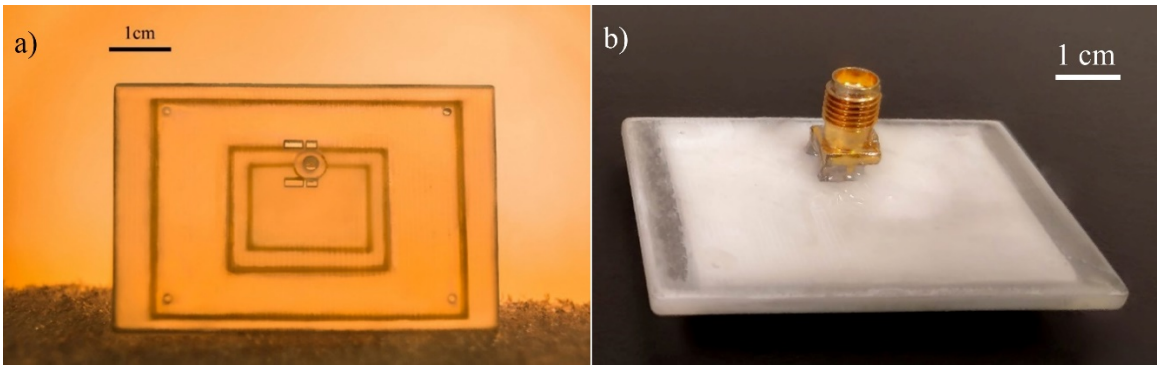

Figure 6.2 a) The actual sample of the 3D printed patch antenna after clearing off the sacrificial support material and b) The fabricated patch antenna with a SMA connector sealed using NOA63 glue.

6.1.4 Results

The fabricated microstrip patch antenna was characterized for its reflection co-efficient, gain, and radiation pattern. The simulated and measured plots of the reflection co-efficient are shown in Figure 6.3. The simulation model shows a good alignment (< 1% error in resonant frequency) with the measured results after including the additional height of sealing glue (NOA63) between the sample and the SMA connector as can be seen from Figure 6.2 (b).

Figure 6.4 illustrates the E and the H-plane section cut (orientation defined in Figure 6.1) of the full 3D radiation pattern for the patch antenna measured with the help of an anechoic chamber at Wireless Research Center of North Carolina (WRCNC). The measured realized gain and the efficiency of the antenna at 6 GHz were 3.51 dBi and 35.8% respectively while the simulated realized gain and total efficiency were 2.94 dBi and 38% respectively.

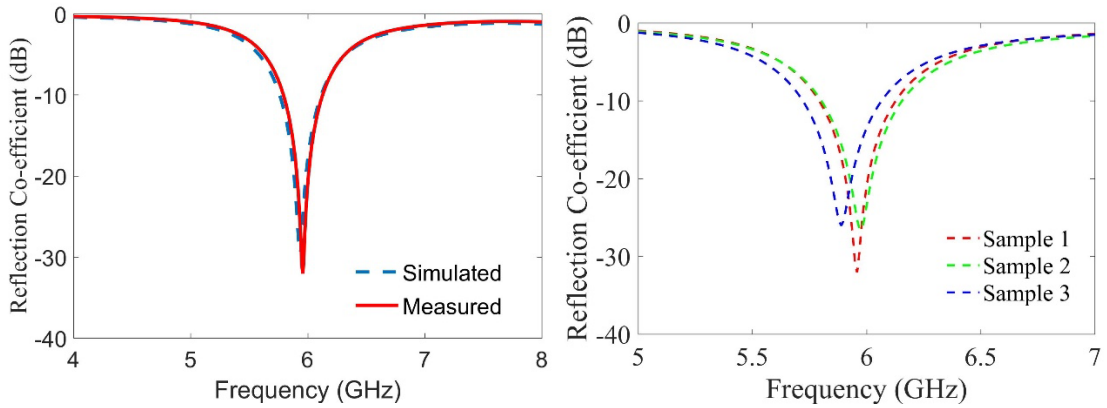

Figure 6.3 a) The measured and simulated reflection co-efficient of the fabricated patch geometry shows a resonance at 5.97 GHz and b) The reflection co-efficient plot for three fabricated samples.

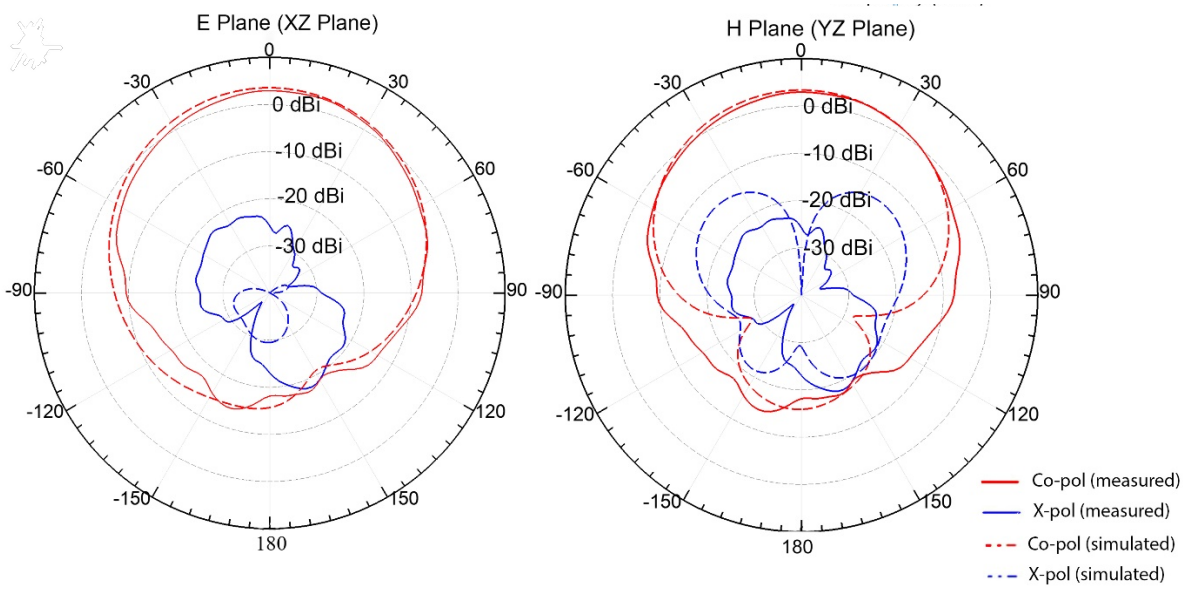

Figure 6.4 The E and H plane co-polarization and cross-polarization radiation pattern for the fabricated antenna and comparison to simulated results.

The simulated total efficiency of the patch antenna was quite low at 38.7% but is within the expectations as the material has a substantially high loss tangent $(\tan\delta)$ of 0.045. The

measured efficiency was 35.8%. The simulations were repeated by changing the loss tangent value of VisiJet M3 Crystal to that of some of the engineered microwave substrates. The geometry for these simulations such as the dimensions of the patch (W, L), ground plane and the height of the patch (h) above the ground plane was kept the same and the simulations also included the resistive losses of EGaIn to gauge the dielectric losses of the substrate. For a substrate with a loss tangent as low as 0.005, the efficiency can be increased to 91% as shown in Table 6.1. Even with lossy conventional substrates such as FR4 with a loss tangent $(\tan\delta)$ of 0.018, the efficiency of the patch antenna can be improved to 61.8%. It brings us to a conclusion that the dominant factor lowering the efficiency of the patch antenna is the dielectric loss mechanism and formulating low loss materials [42] suitable for 3D printing should aid fabrication of highly efficient antenna structures using this metallization technique.

Table 6.1 The comparison of efficiency (simulated) of the microstrip patch structure using EGaIn with VisiJet M3 Crystal and other popular substrates maintaining the same geometry.

Material	Loss tangent $(tan\delta)$	Efficiency η %
VisiJet M3 Crystal	0.045	38.7
FR4	0.018	61.8
Rexolite [42], Rogers Duroid 5880	0.0005	91.1

The measurements were also carried out on three samples of patch antenna in a different anechoic chamber. Lower values of gain was observed with the measurements from this chamber and the discrepancy can be attributed to test antenna calibration error or the presence of a large metallic motor shaft behind the DUT. For the same sample, the gain measured in this anechoic chamber was 2.2 dBi (compared to 3.2 dBi measured at WRCNC). However, the

value of gain and the resonant frequency for the three patch samples were close and as shown in Table 6.2.

Table 6.2 The measured resonant frequency and the gain for the three fabricated patch samples

	Resonant Frequency (GHz)	Gain (dBi)
Sample 1	5.96	2.2
Sample 2	6.02	1.71
Sample 3	5.92	2.32

6.2. Helical Antenna

In this section, the design and fabrication of a helical antenna propagating in axial mode is discussed. Its radiation pattern and axial ratio are also observed and compared to simulations.

6.2.1 Motivation to fabricate helical antenna

Microstrip patch antenna fabricated in the previous section proved the capability of the proposed approach to metalize planar geometries. The goal of the procedure was to be able to build non-planar curved geometries such as a helical filament. To embed a helix inside a dielectric medium, traditional methods of fabrication such as casting and molding can be replaced and simplified with this approach to enable rapid prototyping.

6.2.2 Background

As shown in Figure 6.5, a helical antenna consists of a single conducting wire wound around an axis to form a helix, mounted over a ground plane. The most important parameters concerning the geometry of the helix are its circumference (C), the pitch angle (α), the number

of turns (N) and the spacing between the turns (S) [41]. The pitch angle can be approximately found out using the circumference and turn spacing as,

$$\tan \alpha = \frac{S}{C} \tag{6.5}$$

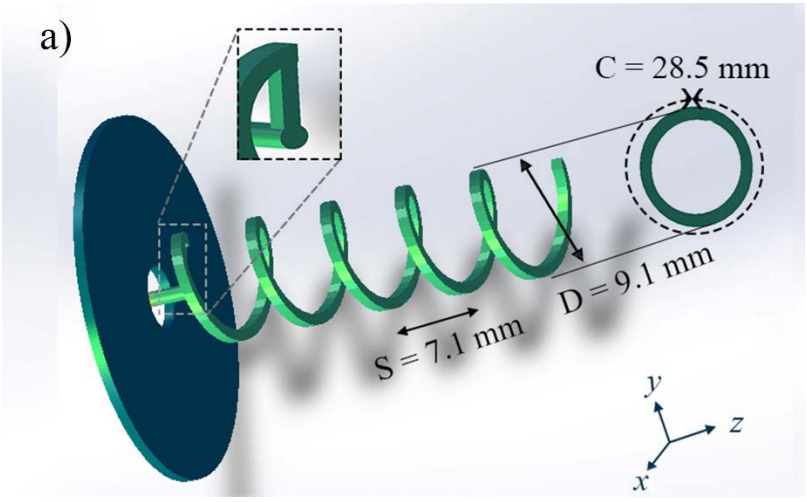

Figure 6.5 Structure of a helical antenna

Helical antennas are popular for their ability to radiate in two distinct modes, the normal mode and the axial mode. The normal mode is linearly polarized and the helix radiates in normal mode when the dimensions of the helix are smaller compared to its electrical length. The direction of maximum radiation in this case is perpendicular to the axis of the helix. The axial mode is a circularly polarized mode and can be excited when the circumference of the helix is comparable to a wavelength in the media. Axial mode helix has its maximum radiation along the axis of the helix. In the axial mode, it forms a traveling wave structure and has properties such as a wide bandwidth, high gain and high directivity [41].

The conventional practice is to have a constant circumference and a pitch angle. Some of the research in the past decade has shown improvements in the axial ratio by using tapered feed end [43], slight improvements in the gain by using curved ground planes [44] or a dual band helix by using a non-uniform pitch angle [45].The peak gain of the antenna can be increased just by increasing the number of turns of the antenna. Helical antennas are capable of providing high gain over a wide range of frequencies.

6.2.3 Design of helical antenna

For a helical antenna radiating in axial mode, the circumference of the helix has to be about a wavelength [29] in the medium.

$$\frac{3}{4}\lambda < C < \frac{4}{3}\lambda \tag{6.6}$$

Around this range the helix operates in axial mode and has a peak gain in the end-fire direction. For 6 GHz, considering the circumference as a wavelength in VisiJet M3 Crystal having a dielectric constant of 3, the diameter of the helix is taken as 9.1 mm. Over the wide range of frequencies, the input impedance will be purely resistive and roughly around

$$R \cong 140\frac{C}{\lambda} \tag{6.7}$$

Since for this design, the circumference has been selected to be equal to the wavelength in the material, the input impedance of the helix at resonant frequency is approximately 140 Ω. This impedance was transformed to 50 Ω by using a small section of a transmission line of width w = 0.74 mm at a height h = 0.53 mm above the ground plane as per an approach proposed by Kraus [46].

From numerous studies, it has been found that the helix has a good performance for a pitch angle around 12º to 14º [41]. For this design, the pitch angle (α) has been selected to be 14º. Figure 6.6 (a) illustrates the sample after support material clearing, Figure 6.6 (b) shows the sealing of the drain hole with NOA 63 and Figure 6.6 (c) demonstrates the helical antenna sample with the attached SMA connector.

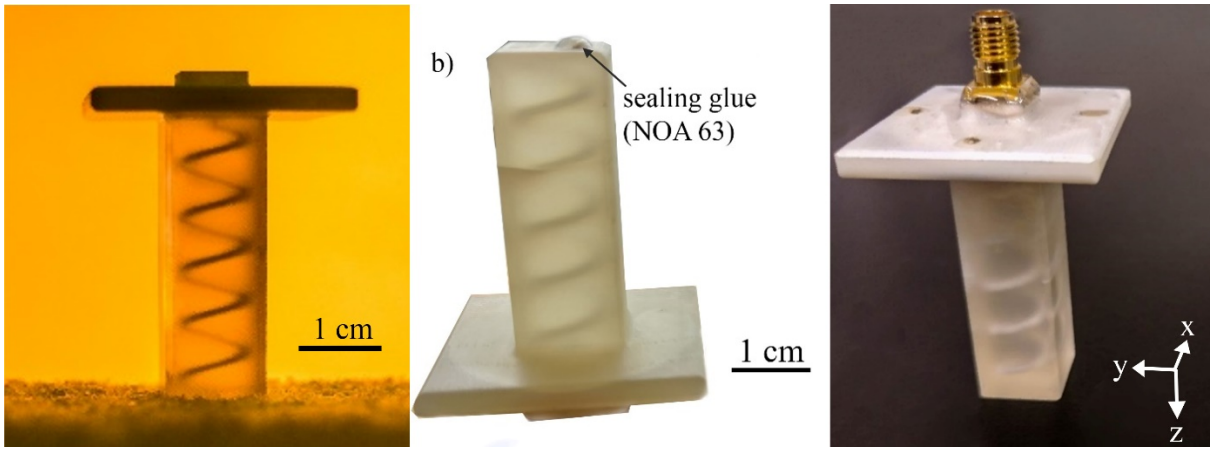

Figure 6.6 a) The actual sample of the 3D printed Helical antenna after clearing off the sacrificial support material, b) The glue added to seal the drain hole and c) The fabricated helical antenna with a SMA connector sealed using NOA63 glue.

6.2.4 Results

Figure 6.7 illustrates the measured and the simulated reflection co-efficient for the designed helical antennas. The plot indicates that the structure has a high bandwidth and that there are two additional resonances between 4-5 GHz. The radiation pattern at these frequencies demonstrates a mix of end-fire and broadside radiations; indicating the presence of a normal mode resonance at these frequencies. The response of the simulation model was close to that of the fabricated antenna with respect to estimating these resonances as well.

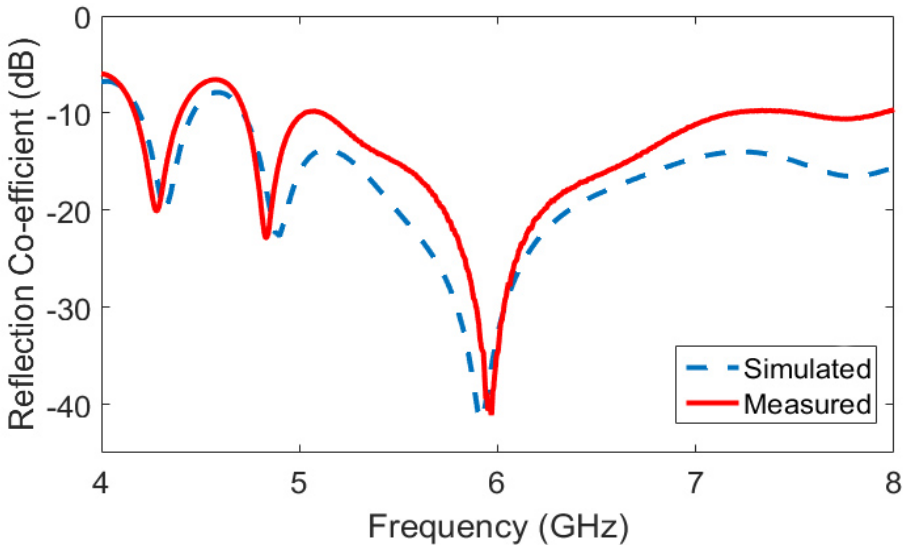

Figure 6.7 The measured and simulated reflection co-efficient of the fabricated patch geometry showing a resonance at 5.96 GHz.

The measurements of the helical antenna carried out at the 3D pattern measurement facility at Wireless Research Center North Carolina (WRCNC) also illustrated the close alignment with respect to the measured normalized radiation patterns as can be seen in Figure 6.8. The measurements were taken using two linearly polarized test antennas measuring the gain along two planes the XZ plane and the YZ plane (axes orientation as defined in Figure 6.5). These two separate measurements were combined to give the total gain and axial ratio for the helical antenna.

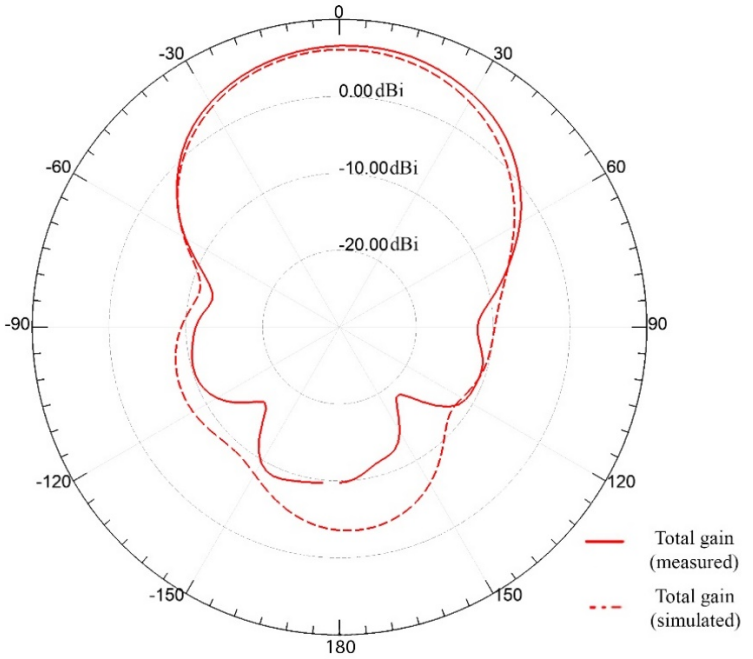

Figure 6.8 The total gain pattern for the fabricated antenna and comparison to simulated results.

The simulated axial ratio for the helical antenna was 1.16 (1.29 dB) while that from measurements was 1.29 (2.2 dB). This variation in the results for the axial ratio relative to the simulated value may be a result of an absence of small amount of the sealing glue as shown in Figure 6.6 (b) in the simulation model. This can cause dielectric loading; however, it is difficult to model this into simulations since it is difficult to exactly determine the thickness of the glue cured for each sample separately. The measured Right Handed Circular Polarization (RHCP) gain of the antenna was 6.54 dBi whereas simulated gain was 6 dBi. The simulated total efficiency of the helical antenna was 61% while the measured efficiency was 53.7%. The small misalignment between the measured and simulated gain and efficiency values can be attributed to the losses experienced due to small amount of sealing glue added between the SMA connector and the helix body similar to the case of microstrip patch antenna

6.3. Microstrip Patch Array

In this section, the motivation and a step by step design procedure for the microstrip patch array fed using co-axial feedline structures is presented. The co-axial feeding network is also built using 3D printing as dielectric medium and liquid metal as the conductors. The results for this array structure are compared to the simulated results.

6.3.1 Motivation for fabricating arrays

With the fabrication of helical antennas, the ability of the process to develop antennas with curved geometry was demonstrated. With the fabrication of arrays, the process could be extended to fabrication of complex geometries involving multiple radiating elements and feed networks. A curved coaxial feed network was selected as the liquid metal had to flow through these channels to fill the individual array elements to test the vacuum-filling procedure for tougher geometries. The ability to fabricate such complex structures can simplify the process of building arrays with a large number of elements. The advantage of having an array fabricated using additive manufacturing is that it can pack both elements and the feed network into a single geometry and would provide precise control over the dimensions.

6.3.2 Background

The small size of microstrip patch antenna limits the control over the radiation pattern. For higher control, an array of patches has to be used. Such an arrangement leads to an increase in the aperture of the antenna leading to improvement in gain and bandwidth. Highly directive patterns can be achieved by precisely spacing the elements of the array such that their far field

radiations interfere constructively for the desired directions and destructively for undesired directions.

For an N element uniform array, the total electric field observed at a point in space is the multiplication of the electric field due to a single element and the array factor. The array factor depends upon a number of conditions such as the number of elements, the spacing between the elements, the wavelength of the excitation wave in the dielectric media, the relative phase shift between the elements and the geometric configuration of the elements.

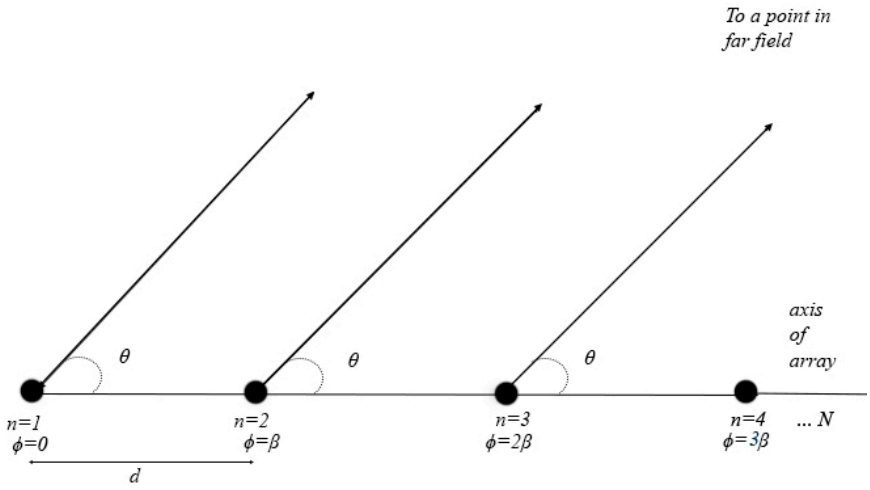

Figure 6.9 An illustration of the general concept of an array of N identical elements arranged uniformly in a linear geometry.

For a uniform linear array of N identical elements as shown in Figure 6.9, the elements spaced at a distance d apart from each other, in a media with propagation constant k and excited with a progressive phase shift of β, the array factor at a point making an angle θ with the normal to the axis of the array can be expressed as [41]

$$AF = \sum_{n=1}^{N} e^{j(n-1)\psi} \tag{6.8}$$

$$\psi = kd\cos\theta + \beta \tag{6.9}$$

As mentioned above, the total radiated field is a multiplication of radiation pattern of an individual element and the pattern of the array factor. As a result, the array factor can introduce dominant side lobes into the radiation field. These lobes are called as grating lobes and they can cause radiation in unnecessary directions or limit the scanning performance of an array. Grating lobes can be avoided by maintaining the spacing between the elements (d) below 0.5λ.

6.3.3 Design of the co-axial transmission line

A coaxial feed line consists of a cylindrical center conductor of diameter d and outer conductor of diameter D. A dielectric medium of dielectric constant ε_r provides insulation between the two conductors as shown in Figure 6.10 (a).

The characteristic impedance of the coaxial transmission line of Z_0 ohms can be fixed by maintaining the ratio of inner diameter d to outer diameter D as per the equation

$$Z_0 \approx \frac{138}{\sqrt{\varepsilon_r}}\log(\frac{D}{d}) \tag{6.10}$$

One small deviation from this equation is the assumption that the material used to implement the transmission line is considered to be lossless which is not true when using dielectric materials and real world conductors. For any practical transmission line, there will be two dominant loss mechanisms – the dielectric losses and the resistive losses of the conductor. For a material with high loss tangent, the dielectric loss mechanism can ruin the performance of the coaxial transmission line.

For the most widely used value of transmission line characteristic impedance of 50 Ω, the ratio D/d needs to be 4.24. Thus, selecting the inner conductor diameter to be 1.3 mm (to ensure proper liquid metal filling inside the cavities) the outer connector diameter should be 5.5 mm.

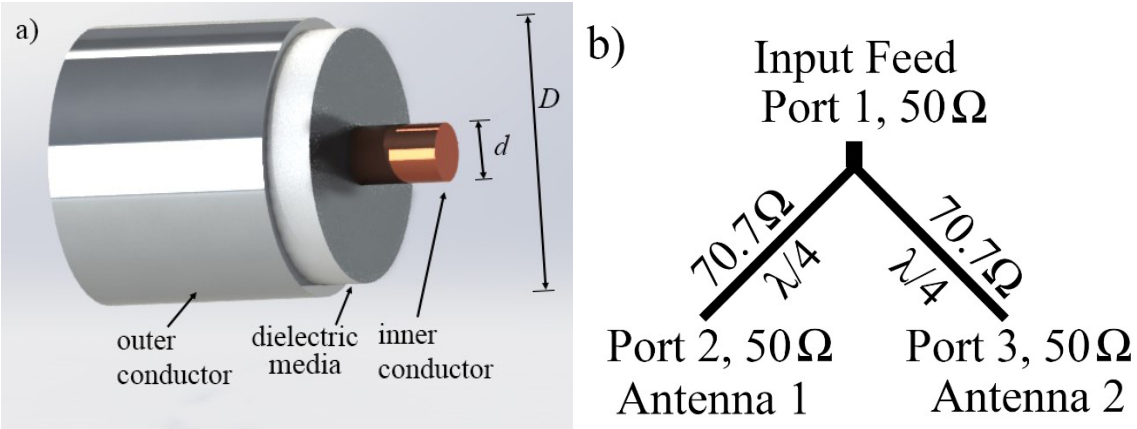

Figure 6.10 a) An illustration of the dimensions and structure of a co-axial line and b) The schematic for a two element T-junction feeding network.

Since the co-axial line feed is also made of VisiJet M3 Crystal which has a high loss tangent at 6 GHz, it is also important to characterize the feed line losses. The loss observed from simulations for a coaxial line made of EGaIn as the conductor and VisiJet M3 Crystal as the dielectric material is 1.4 dB/λ at 6 GHz. For a co-axial transmission line, usually Polyethylene or Teflon (PTFE) is used as the dielectric media. At 6 GHz, the simulated loss using PTFE and liquid metal for the inner and outer conductor is around 0.038 dB/λ.

6.3.4 Design of feed network

Using the co-axial line structure as discussed above, a two-element feeding network can be designed. For a 50 Ω input port feeding two 50 Ω output ports which represent the two

antenna element impedances, the schematic of the feeding network is demonstrated as in Figure 6.10 (b).

A quarter wave transmission line is used for ports 2 and 3 in order to match their impedance of 50 Ω to an impedance of 100 Ω (100 Ω || 100 Ω = 50 Ω at port1). The characteristic impedance of the quarter-wave transmission line Z_{01} for this can be calculated as,

$$Z_{01} = \sqrt{100 \times 50} = 70.7\Omega$$

From the equation 6.10, if the outer conductor diameter is 5.5 mm, the inner conductor diameter has to be 0.71 mm for a characteristic impedance of 70.7 Ω. This simple feeding network is called a T- junction feeding network and is not perfectly matched to a 50 Ω impedance at port 2 and 3. It splits the power equally (-3 dB) to both the output ports. It is not possible to create a lossless perfectly matched feeding network without the introduction of isolation resistors whose inclusion transforms this feeding network into a Wilkinson Power Divider. With the current fabrication methodologies restricting incorporation of resistors into the feed network, a simple T-junction feed network was selected.

It is easy to transform the two-element feeding network discussed above to a four-element feeding network by cascading two T-junction/Wilkinson power divider networks as shown in Figure 6.11 (c). In this case, each output port of the network (port 2,3,4,5) will have equal power which will be 6 dB lower than that at the input port provided that no losses are incurred along the feeding network on account of lossy dielectric or poor conductivity of the two conductors.

The simulations indicate that the power available at the output is about 7.5 dB lower than that incident at the input port (compared to 6 dB for an ideal case). For the designed feed network with VisiJet M3 Crystal as the dielectric medium this poor performance can be attributed to dielectric losses, since we observed a loss of 1.4 dB/λ at 6 GHz. Thus, a four-element array designed with this material will exhibit poor radiation efficiency. However, with proper selection of the printing material, a high-efficiency array can be designed and fabricated in a single package. Figure 6.11 (d) shows the fabricated array.

The inner and outer conductor metallization geometry is illustrated in Figure 6.11 (a). For the co-axial geometry, the inner and outer conductors are in a liquid phase. As a result, if the dielectric medium between the two conductors is not explicitly supported, the block would be free-floating inside the cavity. To reinforce the structure, support structures were added that connect the outer body of the array printed with VisiJet M3 Crystal to the inner dielectric block, also printed with the same material. This arrangement can ensure that the feed network remains fixed and divides the power equally between all its output ports and a constant phase relationship is maintained. This arrangement is illustrated using a cross-sectional view of the array geometry in Figure 6.11 (b).

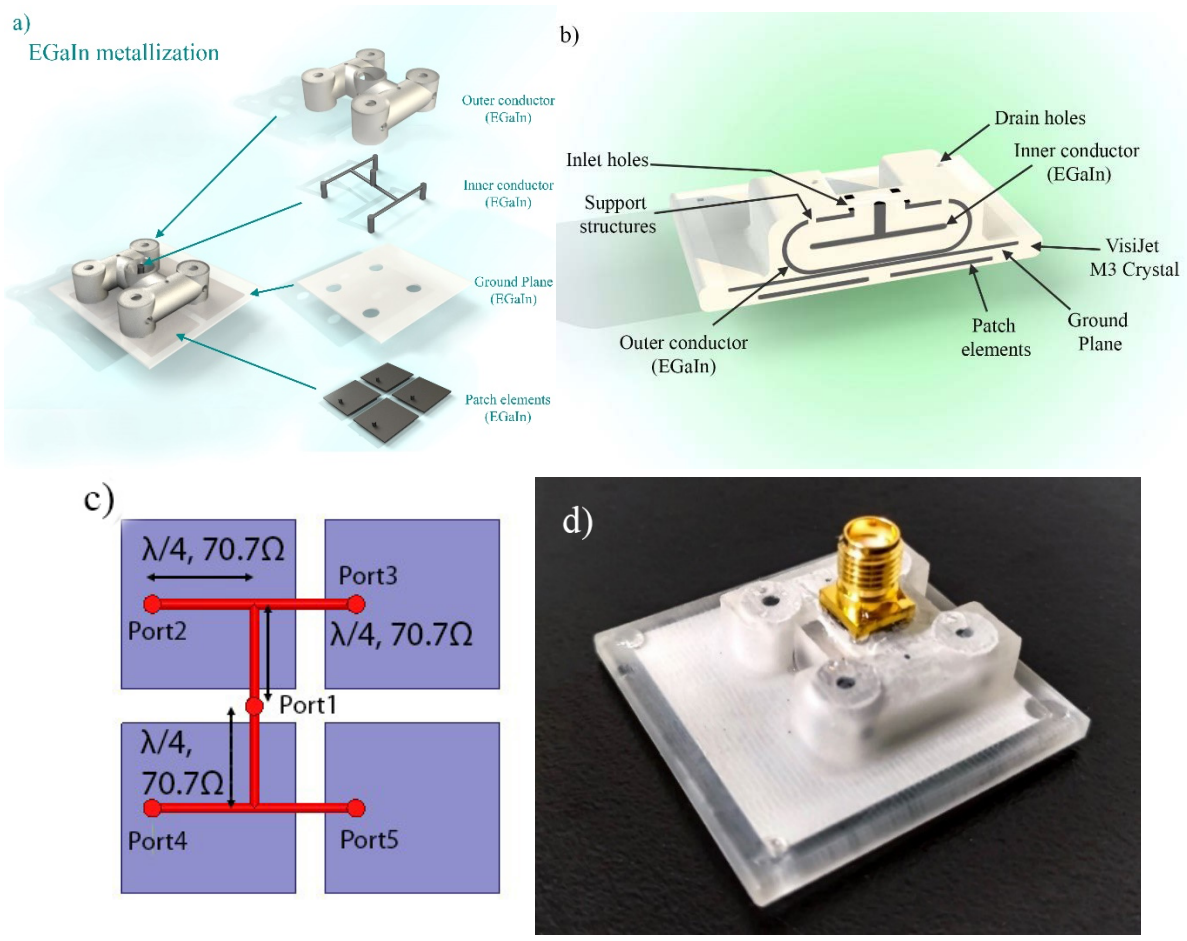

Figure 6.11 a) The exploded view of the metalized parts of the array. This consists of the outer conductor, inner conductor, ground plane and patch elements – all metalized with EGaIn by vacuum filling embedded inside a VisiJet M3 Crystal monolith, b) The cross section cut of the array design illustrating the support structures to hold the dielectric material between the liquid metal filled outer and inner conductors, c) The schematic for the feed network of the microstrip patch array and d) The fabricated micro-strip patch array with a coaxial feed line structure.

6.3.5 Design of a single microstrip patch element

For an array, any radiating structure can be selected as an individual element. For this design, a microstrip patch antenna was selected as an individual element. The design procedure for this antenna is already discussed in section 6.1.3. For each element of the array, the length of the rectangular patch was kept at L = 12.5 mm, width as W = 12 mm, the height from the

ground plane was kept as h = 1 mm. The reduction in the width of the patch was a geometry modification aimed at removing the overlap between the patch elements ($d = 0.5\lambda$) and adding physical separation. The shift in the input impedance of the patch antenna from the 50 Ω was compensated by offsetting the feed by 2.65 mm from the edge of the rectangular patch. Thus, the individual patch antenna elements were matched to 50 Ω impedance of the feed network ports. The array was designed by combining the feed network and four such patch elements.

6.3.6 Results

The reflection co-efficient plot for the fabricated microstrip patch antenna can be seen in Figure 6.12.

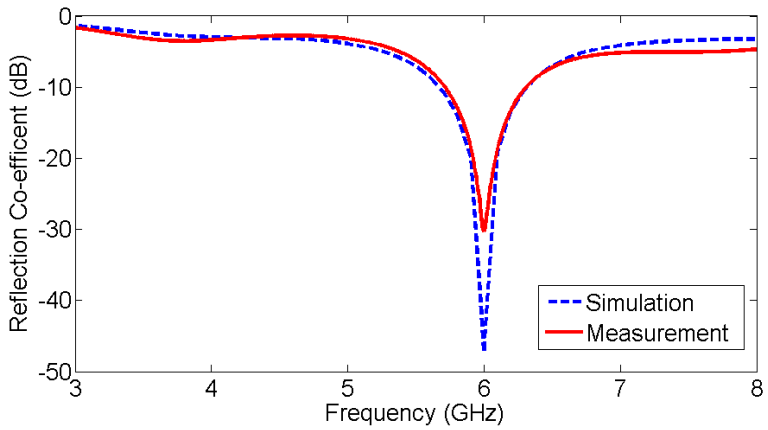

Figure 6.12 The measured and simulated reflection co-efficient of the fabricated patch array geometry shows a resonance at 6 GHz.

The E-plane and the H-Plane co-polarized and cross-polarized radiation pattern plot closely matched the simulations as can be seen in Figure 6.13 with peak gain at broadside, indicating an in-phase excitation of all the four elements. The peak gain observed at the resonant frequency of 6 GHz was 4.17 dBi while the simulation setup indicates a close value of 5 dBi. The simulated total efficiency of the microstrip patch antenna was 47% whereas the

measurements were slightly lower at 41%. Simulated total efficiency for a directly fed single element of the designed four element array was 37%. The total efficiency of the array structure is higher than that of microstrip patch antenna as a consequence of coupling between the elements.

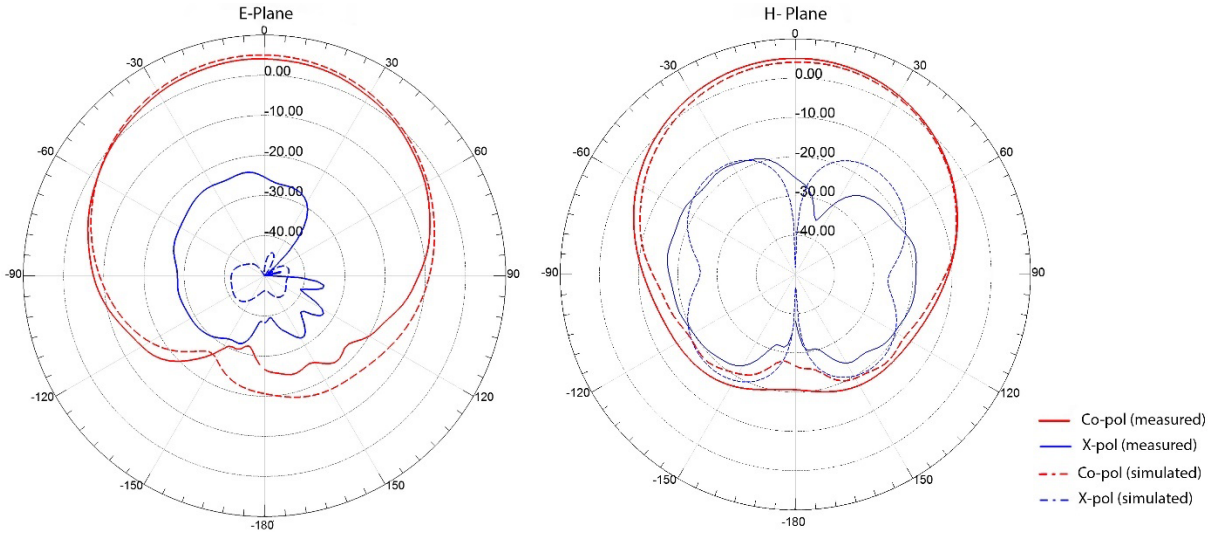

Figure 6.13 The E and H-plane co-polarization and cross-polarization radiation pattern for the fabricated array antenna with broadside radiation and comparison to simulated results.

The close resemblance between the measured and simulated results demonstrate that the procedure can be effectively used to metalize complex curved geometries of the outer conductor, the fine features of the inner conductor and that the vacuum-based filling procedure is able to metalize the individual patch elements effectively even after being forced through narrow inner conductor cavities to get to the patch elements.

In summary, we observe that the vacuum filling approach was able to metalize the geometries with high fidelity. However, there were certain issues faced while fabricating these antennas as discussed in the next chapter.

CHAPTER

7

CHALLENGES AND LIMITATIONS

Improvements to the fabrication process can be found out by understanding the challenges and limitations to the process. While, in principle, the method can be exploited to create components with high dimensional accuracy, the steps required for elimination of the support material, the vacuum-based filling procedure to metalize the geometries with EGaIn and the steps involved for attaching the SMA connector introduce new challenges.

7.1. Support Material Dissolution

In order to examine the feasibility of the 3D printing technique to develop antennas and devices operating at higher range of microwave frequencies, it is necessary to evaluate the best possible resolution achievable. Even though the printer has a layer thickness of 29 µm, the proposed procedure requires a thorough support material dissolution. Incomplete dissolution and removal of support can lead to inconsistencies between the designed and the printed dimensions. Such discrepancies can shift the operating frequency of the fabricated device relative to the simulations and this error will increase at higher frequencies. To assess this, a simple experiment of 3D printing microchannels of varying diameters was set up and the

support material was dissolved using the procedure as discussed in Chapter 5. The time for which the microchannels were kept immersed in EZRinse-C solution and sonication machine was varied from 15 mins to 2 hours. A cross-section cut of the cylindrical microchannels at its outermost tip was observed under a microscope to gauge the radius achieved after the procedure. Figure 7.1 below illustrates the case when the designed microchannel diameter was 500 µm. It can be inferred that the support dissolution improves with increased immersion time in the solvent, however, even after 2 hours of sonication, a support material residue is undissolved causing a discrepancy of 70 µm between designed and measured dimensions.

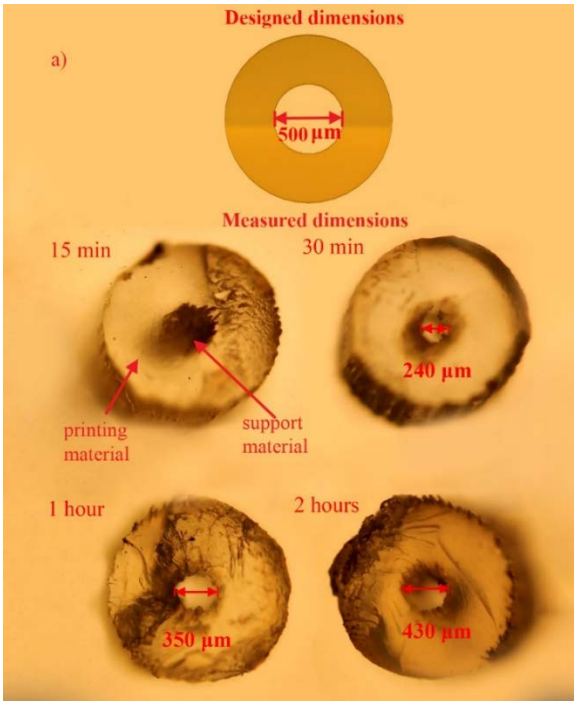

Figure 7.1 The measured inner diameters for the micro-channels approach closer to the designed value of 500 µm as exposure time to warm EZRinse-C solution increases.

For the case of a microchannel diameter of 200 µm, no support material dissolution was observed. The dissolution improves on increasing immersion time, however, it can

increase substantially when more complex geometries are used. This problem can possibly be solved by printing the microchannels in a different orientation, however, the same would not be possible while printing geometries having sharp 90˚ bends for their microchannels or in the case of complex curved non-planar geometries.

7.2. SMA Connector Shorting and EGaIn Leakage

In principle, the fluidic nature of EGaIn can be used to explore applications related to fabrication of reconfigurable antennas. However, it is difficult to interface SMA connectors to the liquid metal-filled antennas. The inability to make a reliable connection from the liquid metal antennas to the RF SMA connectors led to a failure of a few early samples. Improper sealing of the SMA connector to the antenna body using NOA 63 can lead to leakage of EGaIn from the inlet/drain holes and shorting of the SMA connector due to the leaked liquid metal. Figure 7.2 (a) shows EGaIn shorting the center conductor of the SMA to the outer conductors, thereby creating a short circuit at the input of the antenna; Figure 7.2 (b) demonstrates the leakage prone area.

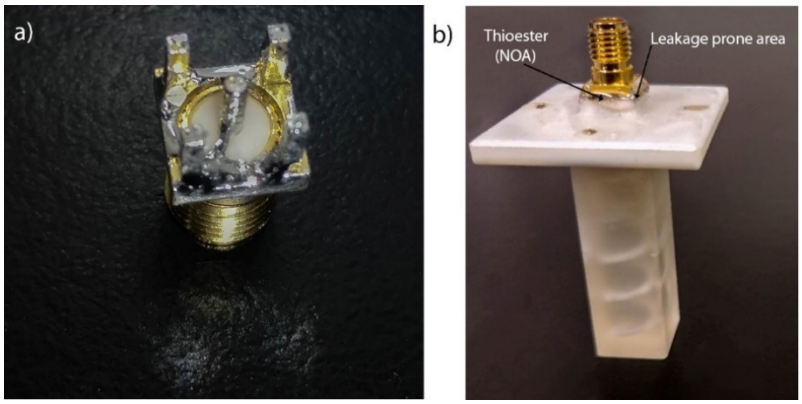

Figure 7.2 a) Shorting of the center conductor to the outer conductor of the SMA connector due to EGaIn and b) The leakage prone area lying at the inlet holes – where the connector is inserted into the 3D printed structure and sealed with sealing glue.

7.3. Efficiency of Vacuum Filling Procedure

The pressure required to fill liquid metal in the cavities embedded inside the 3D printed geometries needs to be determined in order to be able to examine the feasibility of employing vacuum filling process. For a small channel of width W and height h, the pressure required to fill liquid metal into the channel can be found out by using Young-Laplace equation given as [12]

$$P = 2\gamma \cos(\theta)\left(\frac{1}{W} + \frac{1}{h}\right) \tag{7.1}$$

In this equation, the term γ is the measure of interfacial force per unit length of the interface, which for EGaIn, depends upon the mechanical properties of the film and is about 630 mN/m. θ is the contact angle between EGaIn and the interface. It can be clearly observed that the pressure required is inversely proportional to the smallest dimension of the channel, thereby making the process of filling narrow channels challenging using the current methodologies. These calculations are geometry specific and depend upon the dimensions of

the EGaIn inlet, the dimensions of hollow cavities to be metalized and have an additional factor $h\rho g$ to account for the gravity where h is the height of EGaIn above the hollow cavity, ρ is the density of EGaIn and g is the acceleration due to gravity. For the designs presented in chapter 6, a thickness of 500 μm for the array ground plane was tested. Narrower channels could be filled as well and the flow rate can be determined with the help of Computational Fluid Dynamics (CFD) simulations. Such a characterization can help develop design framework and design rules that the antenna designer can follow to create component designs.

7.4. Stability of the Samples over Time and Orientation

The fabricated samples were also tested for their stability over time. Measurements taken after a month on the same patch antenna samples demonstrated a drift in the resonant frequency by a maximum of ~100 MHz. The shift in these resonances may be an effect of change in the shape of the printed structure as a result of heating, cooling, warping or the pressure applied during handling. Since the metal inside can take any shape defined by the hollow cavities and a drift in performance is possible.

As discussed earlier in Chapter 5, it is difficult to accurately determine whether the internal cavities of the printed substrate are completely filled with liquid metal. Voids can appear inside these cavities as a result of improper sealing of the drain holes or the EGaIn reservoir during vacuum filling procedure or while attaching the SMA connector. The presence of such voids can cause orientation-based shifts in the operating frequency of the antenna. An example of this defect (voids) caused as a result of improper sealing of the EGaIn reservoir is

demonstrated with the help of a backlit image in Figure 7.3. However, by ensuring proper sealing, this defect can be avoided.

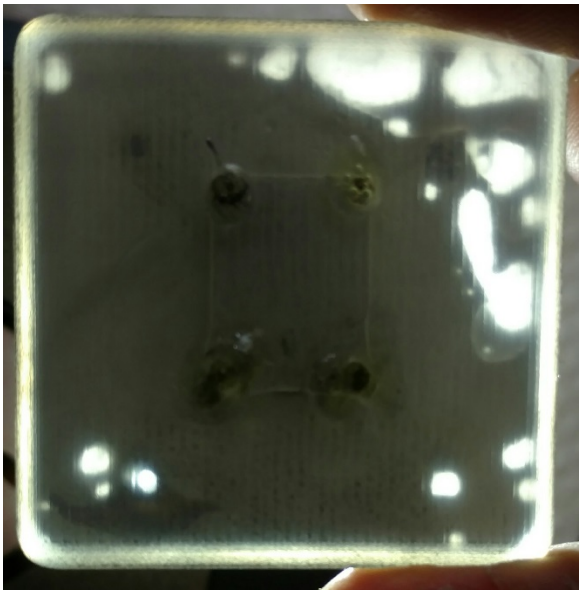

Figure 7.3 A demonstration of an incompletely filled ground plane cavity of the patch antenna. The presence of voids can cause orientation based variations in the performance of the patch over due to the flow of liquid metal inside the cavities.

In summary, the drawbacks and critical limitations of the process introduced in Chapter 5 have been studied. Such an analysis helps us to define the prospective applications of this facile procedure and the further improvements aimed at perfecting the procedure as will be discussed in the next chapter.

CHAPTER

8

CONCLUSION AND FUTURE WORK

In this chapter, we will revisit some of the important highlights of the work. We will also discuss the contributions of this work towards the current research and the prospects for further research on the topic in order to improve the process and other applications.

8.1 Conclusion

The liquid metal vacuum-filling approach has proved to be viable to metalize hollow cavities inside an acrylic 3D printed structure. The technique has been used to metalize a wide range of geometries – planar, non-planar as well as curved to realize RF transmission line and antenna structures with high fidelity. The close alignment of the measured results to the simulated values illustrates the ability of the process to completely metalize the hollow cavities up-to a critical dimension of ~500 µm. The work is a proof of concept demonstration of a versatile approach for the metallization of additively manufactured structures to develop RF devices and antennas.

The dielectric loss mechanism is the dominant loss mechanism for the designed antennas, reducing the efficiency and the gain of the antenna. Research focused on formulation

of low-loss materials suitable for high-resolution 3D printing can help build next-generation high-performance soft devices and antennas. The low loss tangent materials can be used to explore 3D shapes having a large bandwidth and high efficiency while maintaining a compact form factor. The limitations in achieving small features size with high fidelity relative to design dimensions and the pressure requirements to force liquid metal into these cavities would restrict the use of this technique for the higher band of microwave frequencies. However, for the lower range, it provides a means of rapid prototyping a large variety of devices and antennas with complex 3D geometries.

In addition to realizing a single antenna element, the process also allows easy fabrication of a multi-element array design integrated with a feed network. The microstrip patch array design used in this work provides a small increment in the gain compared to the microstrip patch antenna on account of its increased aperture. However, the improvement is not significant because of the dielectric losses incurred in the feed network due to the lossy printing material and can be improved in the future. Such designs can facilitate easy construction of a dimensionally accurate and reconfigurable packaged array structures embedded inside a polymeric substrate in the future.

8.2 Contributions

- The work proposes a versatile approach to metalize planar as well as non-planar 3D printed geometries and a procedure to implement it. 3D printing has the ability to synthesize arbitrary 3D geometries, while the liquid phase of EGaIn provides a simple technique to

develop soft devices near room temperatures. This research combines the advantages both of those methods to fabricate fluidic liquid metal alloy antennas.

- The work also established the feasibility of the liquid metal vacuum-filling approach to fill planar and non-planar curved geometries such as a helical filament achieving performance well aligning with simulations. This ability can help explore arbitrary shaped high performance 3D structures for applications in the field of RF/Microwave and antenna design in the future by providing means to rapid prototype them.
- The array design also illustrates the adaptability of the vacuum filling approach to build multi-element designs with an integrated feed network. Alternative approaches to feed such multi-element designs over the existing widely used microstrip transmission lines can also be explored. This research used an integrated co-axial feed network to feed the four-element array design highlighting the ability to realize curved feedline structures.
- The complex electrical permittivity of VisiJet M3 Crystal using a resonant cavity method is also characterized. The efficiency analysis of the designed antennas illustrates that the printing material is not suitable for designing components at microwave frequencies, since the loss tangent of the material is as high as 0.045.
- The designs used in this approach used a critical dimension of 500 μm for the thickness of planar surfaces for geometries the complex array geometry and microfluidic structures for helical antenna. The work establishes the capability of PolyJet printing to build hollow cavities and metalize small feature sizes and its limitations.
- The limitations of 3D printing pertaining to generating small feature sizes with high accuracy, shorting and leakage issues for SMA connectors have been highlighted.

8.3 Future Work

While the vacuum filling process of embedding liquid metals into 3D printed, acrylic substrates have the advantages of being a simple and quick method of prototyping RF components and antennas; there is still a scope for improvement in order to overcome the limitations stated in Chapter 6 and Chapter 7.

The most principle limitation of the vacuum filling approach is the difficulty in determining the amount of pressure needed to fill the hollow geometries. This pressure not only depends upon the critical dimension of the geometry, but also on the that of the geometry following it, tracing the path of liquid metal into the cavities from the inlet. This can get very tedious when highly integrated, complicated and small feature sized geometries such as phased array designs are concerned. Using Computational Fluid Dynamics (CFD), the pressure requirement can be accurately determined. However, for an antenna design engineer, certain designed rules and framework needs to be formulated to reduce the design time and develop optimized geometries.

As discussed in Chapter 6, one of the limiting factors for this approach was the dominant dielectric loss mechanism of VisiJet M3 Crystal leading to reduced efficiency of the designed antenna structures. With the simulation based efficiency analysis, it was observed that the efficiency of the structure can be increased by a large margin if the loss tangent of the dielectric material was lower. By engineering new printing materials with lower loss tangents capable of high-resolution printing, highly efficient antennas can be designed. In addition to developing materials with superior electrical characteristics, an improvement in the mechanical characteristics of the material such as warping and deformation on application of strain can

also benefit designs for rigid components. Dynamic shifts in performance over time or orientation can be combatted by improving their resistance to higher temperatures and pressure once printed and cured.

One major issue that invites more research is the methodology used to interface the liquid metals to the SMA connectors. While interfacing continued to be one of the most critical issues for fabricating the antenna, it can surely benefit from an alternate design of the SMA connectors eliminating leakage at the interface. Such arrangements can reduce the problems associated with the shorting of the connectors as well.

The fluidic nature of liquid metal inside the cavities encourages the incorporation of scanning performance for the array design based on introducing variations in the feeding network to get progressive phase shifts. This can be realized either by pneumatics-based or by electro-chemistry based flowing of liquid metals inside the cavities. Such an arrangement can be exploited to create beam-steering arrays. Alternatively, it can also be used to construct conformal and/or reconfigurable geometries. While liquid metals have been used to design reconfigurable geometries as discussed in Chapter 1, more research will be oriented towards being able to print stretchable and wearable electronics, sensors, RF devices and antennas using additive manufacturing and will greatly benefit from the use of liquid metals developing custom geometries.

REFERENCES

[1] I. Gibson, D. Rosen, and B. Stucker, *Additive Manufacturing Technologies*. New York, NY: Springer New York, 2015.

[2] K. V. Wong and A. Hernandez, "A Review of Additive Manufacturing," *Int. Sch. Res. Not.*, vol. 2012, p. e208760, Aug. 2012.

[3] L. E. Murr *et al.*, "Next-generation biomedical implants using additive manufacturing of complex, cellular and functional mesh arrays," *Philos. Trans. R. Soc. Lond. Math. Phys. Eng. Sci.*, vol. 368, no. 1917, pp. 1999–2032, Apr. 2010.

[4] L. E. Murr, S. M. Gaytan, E. Martinez, F. Medina, and R. B. Wicker, "Next generation orthopaedic implants by additive manufacturing using electron beam melting," *Int. J. Biomater.*, vol. 2012, p. 245727, 2012.

[5] I. Campbell, D. Bourell, and I. Gibson, "Additive manufacturing: rapid prototyping comes of age," *Rapid Prototyp. J.*, no. 18(4), pp. 255–258, 2012.

[6] J.-P. Kruth, M. C. Leu, and T. Nakagawa, "Progress in Additive Manufacturing and Rapid Prototyping," *CIRP Ann. - Manuf. Technol.*, vol. 47, no. 2, pp. 525–540, Jan. 1998.

[7] E. G. Geterud, P. Bergmark, and J. Yang, "Lightweight waveguide and antenna components using plating on plastics," in *2013 7th European Conference on Antennas and Propagation (EuCAP)*, 2013, pp. 1812–1815.

[8] J. J. Adams *et al.*, "Conformal Printing of Electrically Small Antennas on Three-Dimensional Surfaces," *Adv. Mater.*, vol. 23, no. 11, pp. 1335–1340, Mar. 2011.

[9] W. E. Frazier, "Metal Additive Manufacturing: A Review," *J. Mater. Eng. Perform.*, vol. 23, no. 6, pp. 1917–1928, Apr. 2014.

[10] S.-Y. Wu, C. Yang, W. Hsu, and L. Lin, "3D-printed microelectronics for integrated circuitry and passive wireless sensors," *Microsyst. Nanoeng.*, vol. 1, p. 15013, Jul. 2015.

[11] Y. Kosta and S. Kosta, "Liquid antenna systems," in *IEEE Antennas and Propagation Society International Symposium, 2004*, 2004, vol. 3, p. 2392–2395 Vol.3.

[12] M. D. Dickey, R. C. Chiechi, R. J. Larsen, E. A. Weiss, D. A. Weitz, and G. M. Whitesides, "Eutectic Gallium-Indium (EGaIn): A Liquid Metal Alloy for the Formation of Stable Structures in Microchannels at Room Temperature," *Adv. Funct. Mater.*, vol. 18, no. 7, pp. 1097–1104, Apr. 2008.

[13] M. Wang, C. Trlica, M. R. Khan, M. D. Dickey, and J. J. Adams, “A reconfigurable liquid metal antenna driven by electrochemically controlled capillarity,” *J. Appl. Phys.*, vol. 117, no. 19, p. 194901, May 2015.

[14] “Tedpella silver Paste; URL: https://www.tedpella.com/technote_html/16032TN.pdf.”

[15] G. J. Hayes, Ju-Hee So, A. Qusba, M. D. Dickey, and G. Lazzi, “Flexible Liquid Metal Alloy (EGaIn) Microstrip Patch Antenna,” *IEEE Trans. Antennas Propag.*, vol. 60, no. 5, pp. 2151–2156, May 2012.

[16] A. Vorobyov, C. Henemann, and P. Dallemagne, “Liquid Metal based antenna for wearable electronic,” in *2016 10th European Conference on Antennas and Propagation (EuCAP)*, 2016, pp. 1–3.

[17] H. Pan, “Liquid Metal Reconfigurable Antennas,” Texas A&M University, USA, 2016.

[18] J. T. Bernhard, “Reconfigurable Antennas,” *Synth. Lect. Antennas*, vol. 2, no. 1, pp. 1–66, Jan. 2007.

[19] M. Cosker, F. Ferrero, L. Lizzi, R. Staraj, and J. M. Ribero, “3D flexible antenna realization process using liquid metal and additive technology,” in *2016 IEEE International Symposium on Antennas and Propagation (APSURSI)*, 2016, pp. 809–810.

[20] J. Stampfl and M. Hatzenbichler, “Additive Manufacturing Technologies,” in *CIRP Encyclopedia of Production Engineering*, L. Laperrière, G. Reinhart, and T. I. A. for P. Engineering, Eds. Springer Berlin Heidelberg, 2014, pp. 20–27.

[21] “Projet 3500HDMax manual; URL: http://www.3dsystems.com/sites/www.3dsystems.com/files/projet_3500_plastic_0115_usen_web.pdf.”

[22] “Materials and Accessories Overview; URL: http://www.3dsystems.com/materials/production.” 3D Systems.

[23] “PolyJet Materials Datasheet, URL: http://usglobalimages.stratasys.com/Main/Files/Material_Spec_Sheets/MSS_PJ_PJMaterialsDataSheet.pdf?v=635785205440671440.” Stratasys Ltd.

[24] W. Sha, X. Wu, and K. G. Keong, *Electroless Copper and Nickel-Phosphorus Plating: Processing, Characterisation and Modelling*. Elsevier, 2011.

[25] P. A. Flinn, D. S. Gardner, and W. D. Nix, “Measurement and Interpretation of stress in aluminum-based metallization as a function of thermal history,” *IEEE Trans. Electron Devices*, vol. 34, no. 3, pp. 689–699, Mar. 1987.

[26] S. B. Walker and J. A. Lewis, “Reactive Silver Inks for Patterning High-Conductivity Features at Mild Temperatures,” *J. Am. Chem. Soc.*, vol. 134, no. 3, pp. 1419–1421, Jan. 2012.

[27] P. T. Timbie, J. Grade, D. van der Weide, B. Maffei, and G. Pisano, “Stereolithographed MM-wave corrugated horn antennas,” in *2011 36th International Conference on Infrared, Millimeter and Terahertz Waves (IRMMW-THz)*, 2011, pp. 1–3.

[28] B. I. Wu and I. Ehrenberg, “Ultra conformal patch antenna array on a doubly curved surface,” in *2013 IEEE International Symposium on Phased Array Systems Technology*, 2013, pp. 792–798.

[29] F. Cai, W. T. Khan, and J. Papapolymerou, “A low loss X-band filter using 3-D Polyjet technology,” in *2015 IEEE MTT-S International Microwave Symposium*, 2015, pp. 1–4.

[30] G. A. Casula, G. Montisci, and G. Mazzarella, “A Wideband PET Inkjet-Printed Antenna for UHF RFID,” *IEEE Antennas Wirel. Propag. Lett.*, vol. 12, pp. 1400–1403, 2013.

[31] B. J. Willis, “Compact form fitting small antennas using three-dimensional rapid prototyping.” The University of Utah, 2012.

[32] M. Liang, Xiaoju Yu, C. Shemelya, E. MacDonald, and H. Xin, “3D printed multilayer microstrip line structure with vertical transition toward integrated systems,” 2015, pp. 1–4.

[33] M. Cosker, F. Ferrero, L. Lizzi, R. Staraj, and J. M. Ribero, “3D flexible antenna realization process using liquid metal and additive technology,” in *2016 IEEE International Symposium on Antennas and Propagation (APSURSI)*, 2016, pp. 809–810.

[34] C. Balanis, *Advanced Engineering Electromagnetics*, 2nd Edition. Wiley Publication House.

[35] H. E. Bussey, “Measurement of RF properties of materials a survey,” *Proc. IEEE*, vol. 55, no. 6, pp. 1046–1053, Jun. 1967.

[36] J. M. Heinola, P. Silventoinen, K. Latti, M. Kettunen, and J. P. Strom, “Determination of dielectric constant and dissipation factor of a printed circuit board material using a microstrip ring resonator structure,” in *15th International Conference on Microwaves, Radar and Wireless Communications, 2004. MIKON-2004*, 2004, vol. 1, p. 202–205 Vol.1.

[37] T. Chiu, “Dielectric constant measurement technique for a dielectric strip using a rectangular waveguide,” *IEEE Trans. Instrum. Meas.*, vol. 52, no. 5, pp. 1501–1508, Oct. 2003.

[38] A. D. Yaghjian and S. R. Best, “Impedance, bandwidth, and Q of antennas,” *IEEE Trans. Antennas Propag.*, vol. 53, no. 4, pp. 1298–1324, Apr. 2005.

[39] B. I. Wu and I. Ehrenberg, “Ultra conformal patch antenna array on a doubly curved surface,” in *2013 IEEE International Symposium on Phased Array Systems Technology*, 2013, pp. 792–798.

[40] H. Iwasaki, “A circularly polarized small-size microstrip antenna with a cross slot,” *IEEE Trans. Antennas Propag.*, vol. 44, no. 10, pp. 1399–1401, Oct. 1996.

[41] C. Balanis, *Antenna Theory Analysis and Design,* 3rd Edition. .

[42] M. Lis *et al.*, “Polymer Dielectrics for 3D-Printed RF Devices in the Ka Band,” *Adv. Mater. Technol.*, vol. 1, no. 2, p. n/a-n/a, May 2016.

[43] J. Yamauchi, H. Nakano, and H. Mimaki, “Backfire bifilar helical antenna with tapered feed end,” in *Antennas and Propagation Society International Symposium, 1981*, 1981, vol. 19, pp. 683–686.

[44] A. R. Djordjevic, A. G. Zajic, and M. M. Ilic, “Enhancing the gain of helical antennas by shaping the ground conductor,” *IEEE Antennas Wirel. Propag. Lett.*, vol. 5, no. 1, pp. 138–140, Dec. 2006.

[45] G. Zhou, “A non-uniform pitch dual band helix antenna,” in *IEEE Antennas and Propagation Society International Symposium, 2000*, 2000, vol. 1, pp. 274–277 vol.1.

[46] J. Kraus, “A 50-ohm input impedance for helical beam antennas,” *IEEE Trans. Antennas Propag.*, vol. 25, no. 6, pp. 913–913, Nov. 1977.